

DESIGN AND IMPLEMENTATION OF AN ACTUATED PROBE SUITE FOR AN ORIFICED HOLLOW CATHODE

JORDAN BROWN, '18

SUBMITTED TO THE
DEPARTMENT OF MECHANICAL AND AEROSPACE ENGINEERING
PRINCETON UNIVERSITY
IN PARTIAL FULFILLMENT OF THE REQUIREMENTS OF
UNDERGRADUATE INDEPENDENT WORK.

FINAL REPORT

MAY 2, 2018

EDGAR CHOEIRI
JULIA MIKHAILOVA
MAE 442
70 PAGES
ADVISER COPY

© Copyright by Jordan Brown, 2018.
All Rights Reserved

This thesis represents my own work in accordance with University regulations.

Abstract

A system of diagnostics consisting of a reciprocating triple probe was developed to measure the axial variation of the plasma density within an orificed hollow cathode. The system was created to validate a charge-exchange-limited diffusion model. Finite element models were created to ensure that the thermal and mechanical loads of steady-state cathode operation do not destroy or deform the structure. The reciprocating probe is actuated by a vacuum-rated stepper motor. A visual interface and controller was programmed in Labview to fully automate the system and track the position of the probe. The system was fabricated using computer-aided manufacturing techniques, and assessed during cathode operation.

During operation, the position of the probe can traverse the active zone of the cathode in 2.5 seconds. Its position was tracked at a maximum rate of 30 queries per second. The system was tested under a vacuum of 10^{-5} torr, where a plasma was generated in the cathode. Steady-state operation was not achieved, and probe measurements were unable to be performed. The system experienced no deformation from the cathode initialization, indicating that the system is capable of withstanding the thermal and mechanical loads of steady-state operation. The diagnostics will be used for further experimentation within the Electric Propulsion and Plasma Dynamics Laboratory of Princeton University.

Acknowledgements

I would like to thank several people for assisting me in the creation of this thesis. Without their support, none of these pages would have been possible.

First I would like to express my gratitude to Professor Choueiri, who welcomed me into his lab and has provided countless opportunities for me to develop my scientific understanding.

Next, I would like to thank the other members of the EP lab: Chris Wordingham, Will Coogan, Sebastian Rojas Mata, and Pierre-Yves Taunay. In particular, I would like to thank Pierre-Yves, who has offered his continual assistance and guidance in all aspects of this thesis.

Outside of the EP lab, I would like to extend thanks to several members of the MAE staff. To Glenn Northey and Al Gaillard, who assisted me in machining and manufacturing on countless occasions. To Jon Prevost, who advised me in selecting a motor, and provided me the electronics background to understand and control the motor and probes. To Professor Arnold, who offered his advice in understanding the thermal analysis for this thesis. To Jo Ann Kropilak-Love, for the continual logistical support she provided throughout the year. And to all of my Princeton Professors, who have provided me an academic background that has not only enabled me to complete this thesis, but will also qualify me to face greater challenges in the future.

I would also like to acknowledge my friends, who have made my Princeton experience so enjoyable. Foremost, I would like to thank The Princeton Quadrangle Club as a whole. Quad has both provided me a Princeton home and has facilitated my growth as a person and as a leader. It has introduced me to many friends whom I will never forget, and many experiences I will always remember. In particular, I would like to thank my best friend Elizabeth Meyers, who has proofread and otherwise assisted me in writing this thesis, and who has made the past year and a half phenomenal. FCFCQQQ

Finally, I would like to express my gratitude towards my Mom and Dad. They have supported me in all of my endeavors, both academically and otherwise, and I will forever appreciate the positive upbringing, for which they are responsible.

This thesis was made possible by the John Marshall II Memorial Prize Fund and the Department of Mechanical and Aerospace Engineering. The generous funding provided by these sources allowed me create a thesis of this complexity, and for this support I am thankful.

To Infinity and Beyond

Contents

| | |
|--|----------|
| Abstract | iii |
| Acknowledgements | iv |
| List of Tables | viii |
| List of Figures | ix |
| List of Symbols | xi |
| 1 Introduction | 1 |
| 1.1 Electric Propulsion | 1 |
| 1.2 Orificed Hollow Cathodes | 3 |
| 1.2.1 General Principles | 3 |
| 1.2.2 Attachment Length | 4 |
| 1.3 Probe Theory | 4 |
| 1.3.1 Plasma Sheaths | 4 |
| 1.3.2 Triple Probes | 6 |
| 1.3.3 Emissive Probes | 7 |
| 1.4 Purpose | 7 |
| 2 Design Process | 9 |
| 2.1 Design Parameters | 9 |
| 2.1.1 Experimental Setup | 9 |
| 2.1.2 Problem Statement | 11 |
| 2.2 Overarching Schematic | 12 |
| 2.2.1 Previous Work | 12 |
| 2.2.2 Conceptual Approach | 13 |
| 2.3 Structural Design | 14 |
| 2.3.1 Material Selection | 16 |
| 2.4 Circuitry & Probes | 17 |
| 2.4.1 Circuitry | 17 |
| 2.4.2 Design & Construction | 18 |

| | | |
|----------|--------------------------------------|-----------|
| 2.5 | Motor Selection | 20 |
| 2.5.1 | Selection Criteria | 20 |
| 2.5.2 | Performance Specifications | 23 |
| 2.5.3 | Programming | 24 |
| 3 | Thermal Modeling | 27 |
| 3.1 | Initialization | 27 |
| 3.1.1 | Material Properties | 27 |
| 3.1.2 | Case Studies | 28 |
| 3.2 | Temperature Analysis | 31 |
| 3.3 | Stress Analysis | 34 |
| 3.3.1 | Thermal Stresses | 35 |
| 3.3.2 | Mechanical Stresses | 37 |
| 3.4 | Summary | 37 |
| 4 | Results and Discussion | 39 |
| 4.1 | Final Design | 39 |
| 4.2 | Experimental Results | 41 |
| 4.3 | Discussion | 43 |
| 4.3.1 | Future Work | 43 |
| 4.3.2 | Conclusion | 46 |
| A | CAD Drawings | 49 |
| B | Motor Schematics | 56 |
| B.1 | Actuation Code | 56 |
| C | Budget | 58 |

List of Tables

| | | |
|-----|--|----|
| 2.1 | List of Parts for Figure 2.6 | 16 |
| 2.2 | Part materials for diagnostics subsystem structure. | 18 |
| 2.3 | Dimensions and melting temperatures of the probe materials. | 20 |
| 3.1 | Equation constants for the thermal conductivity and heat capacity of the materials. | 28 |
| 3.2 | Categorization of the studies performed. | 31 |
| B.1 | Explanation of the command string used to control the stepper motor. | 57 |

List of Figures

| | | |
|------|--|----|
| 1.1 | Cutaway view of a typical orificed hollow cathode | 2 |
| 1.2 | Regions and important variables labeled on a probe characteristic . . | 5 |
| 2.1 | Yellow fiberglass tank used in the Pulsed High-Power Performance Facility of the EPPDyL. | 10 |
| 2.2 | The graphite cathode and RA253MA steel base plate. | 11 |
| 2.3 | The hollow cathode test configuration used by Siegfried and Wilbur. . | 12 |
| 2.4 | Pneumatic scanning probe and dual bellows design created by Goebel et al. | 13 |
| 2.5 | Multiple views of the assembly for the final design. The cathode tube and base plate are colored in blue and black respectively. | 15 |
| 2.6 | Labeled cutaway diagram of the diagnostics subsystem. Cathode is axially symmetric with respect to orifice axis. | 16 |
| 2.7 | Several parts of the diagnostics subsystem. Parts measure 4 inches to a side. | 17 |
| 2.8 | Circuit Design to control the triple probe. | 19 |
| 2.9 | Design schematic of the combined Triple - Emitter Probe. | 20 |
| 2.10 | Probe slider supported by the leadscrew and guiding rod. See Appendix A.11 for scale. | 21 |
| 2.11 | Photo of the combined probe. | 21 |
| 2.12 | The diagnostics port and Amphenol connector. For detailed drawings of the port and clamp, see Appendix A.12 and A.13. | 22 |
| 2.13 | The 211-18-01 vacuum rated stepper motor. See Appendix B.1 for scale. | 23 |
| 2.14 | Back View | 24 |
| 2.15 | The stepper motor mounted to the diagnostics subsystem frame. . . . | 24 |
| 2.16 | Torque Curve for the 211-18-01 vacuum rated stepper motor. | 25 |
| 2.17 | Labview schematic to control the stepper motor. | 26 |

| | | |
|------|--|----|
| 3.1 | Trend lines for the thermal conductivity of aluminum and austenitic steel. | 29 |
| 3.2 | Trend lines for the heat capacity of aluminum and austenitic steel. . . | 29 |
| 3.3 | Temperature and thermal stress simulations without active cooling. . | 30 |
| 3.4 | Temperature analysis conducted using Autodesk Fusion 360 on an early design model. | 32 |
| 3.5 | Thermal models of each of the studies performed. Color scale is capped at 800 K to show variance in temperature. | 33 |
| 3.6 | Maximum temperatures attained in the modular plate and probe hangar. | 34 |
| 3.7 | Thermal stress models of each of the studies performed. Stresses capped at 300 MPa to show variance across model | 36 |
| 3.8 | Maximum stresses attained in the modular plate. | 37 |
| 3.9 | Mechanical stresses of the system due to gravity. | 38 |
| 4.1 | The final diagnostics subsystem design. | 40 |
| 4.2 | Calibration curve for 12000 steps. | 41 |
| 4.3 | The final design implemented into the experimental setup. | 42 |
| 4.4 | The cathode in operation within the fiberglass tank. | 43 |
| 4.5 | The diagnostics assembly after the experiment. | 44 |
| 4.6 | Modified probe hangar to improve the wiring and fastening. | 45 |
| A.1 | CAD drawing of the Base Plate | 49 |
| A.2 | CAD drawing of a Orificed Hollow Cathode | 50 |
| A.3 | CAD drawing of the Clamp Ring | 50 |
| A.4 | CAD drawing of the Emitter | 51 |
| A.5 | CAD drawing of the Modular Plate | 51 |
| A.6 | CAD drawing of the Probe Hangar | 52 |
| A.7 | CAD drawing of the Motor Plate | 52 |
| A.8 | CAD drawing of the Motor Chamber | 53 |
| A.9 | CAD drawing of the End Plate | 53 |
| A.10 | CAD drawing of the Guide Rod | 54 |
| A.11 | CAD drawing of the Slider Body | 54 |
| A.12 | CAD drawing of the Diagnostics Port Cover | 55 |
| A.13 | CAD drawing of the Diagnostics Port Clamp | 55 |
| B.1 | Engineering Drawing | 56 |

List of Symbols

| | | |
|-----------------|--|----|
| V | Velocity | 1 |
| I_{sp} | Specific impulse | 1 |
| g_0 | Acceleration due to gravity at Earth's surface | 1 |
| m | Mass | 1 |
| j | Current Density | 3 |
| T | Emitter Temperature | 3 |
| ϕ | Work Function | 3 |
| k_B | Boltzmann Constant | 3 |
| T_e | Electron Temperature | 6 |
| k_B | Boltzmann Constant | 6 |
| n_e | Electron Density | 6 |
| A_p | Projected Probe Area | 6 |
| C | Probe Geometry Constant | 6 |
| G | Gain | 18 |
| R | Resistance | 18 |
| τ | Torque required to rotate lead-screw | 21 |
| l | Travel distance per turn | 21 |
| d_m | Lead-screw diameter | 21 |
| μ | Coefficient of friction | 21 |
| F | Load on lead-screw | 21 |
| x | Total travel distance | 22 |
| t | Total time of travel | 22 |
| σ_x | Uncertainty in position | 24 |
| n | Number of steps | 24 |
| σ_{\max} | Ultimate tensile strength | 28 |
| Nu_D | Nusselt number | 32 |
| k | Thermal conductivity | 32 |
| α_L | Coefficient of linear expansion | 35 |

Chapter 1

Introduction

Plasmas are characterized as an ionized, quasineutral gases that exhibits collective behavior dominated by the effects of the long-range electric and magnetic fields [6]. Cathodes are a crucial part of electric propulsion, where they generate plasmas and neutralize plasma beams created from specific electric propulsion devices. To measure the properties of a plasma, a specialized set of tools and techniques are required, which are commonly referred to as *plasma diagnostics*. This chapter will explain the fundamentals of electric propulsion, orificed hollow cathodes, and several relevant plasma diagnostics techniques in order to provide background for the diagnostics design decisions discussed later.

1.1 Electric Propulsion

Nearly all forms of spacecraft propulsion rely on Newton's second and third law to accelerate. Chemical thrusters create energy through combustion reactions, heating the chemical products as a result. The resulting heated gas is accelerated as it expands through the nozzle, which generates thrust for the spacecraft. This creates a change in velocity, ΔV , which enables spacecraft to perform various maneuvers. However, chemical propulsion is limited by the large propellant mass required to produce large ΔV , as the Tsiolkovsky rocket equation demonstrates:

$$\Delta V = I_{sp} g_0 \ln \frac{m_0}{m_f} \quad (1.1.1)$$

Here I_{sp} is the specific impulse of the rocket, $\frac{m_0}{m_f}$ is the ratio of initial and final masses of the spacecraft, and g_0 is the acceleration due to gravity at Earth's surface.

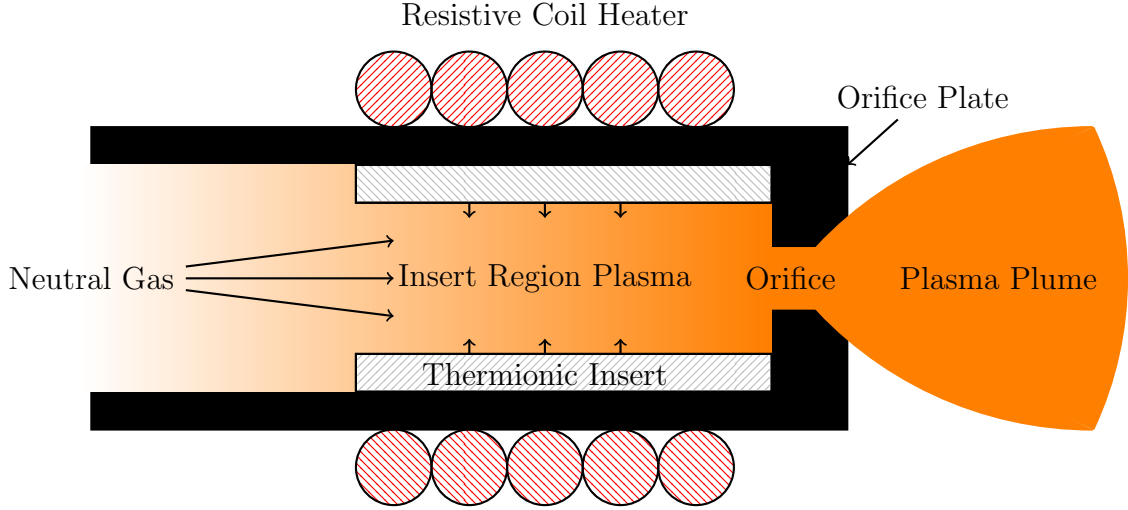


Figure 1.1: Cutaway view of a typical orificed hollow cathode

Presently, the I_{sp} of advanced chemical rockets does not far exceed 450 s, with the Delta IV Heavy measuring an I_{sp} of 465 s [23]. A hypothetical mission from low Earth orbit to Mars' orbit would require a ΔV of at least 5.93 km/s. A chemical rocket with an I_{sp} of 450 s would require that nearly 74% of the rocket's mass be propellant. Without radically improving the I_{sp} of a spacecraft, similar deep-space missions would be costly and inefficient.

Electric propulsion typically produces an order of magnitude higher I_{sp} than chemical propulsion. Of particular importance for this thesis are Hall and ion thrusters, which may have I_{sp} as high as 1500 s and 5000 s respectively [22]. For thrusters of these specifications, the required propellant mass percentages would be reduced to 33% and 11%; a vast improvement from their chemical propulsion counterparts.

While electric propulsion is unable to provide the sheer thrust required to escape Earth, it is a much more mass-efficient option once a spacecraft is in orbit. Since electric propulsion is unable to provide the large impulsive thrusts of chemical propulsion, it must continually function to supply the required ΔV . As such, the operational lifetime often ends up limiting the use of these electric propulsion solutions.

1.2 Orificed Hollow Cathodes

1.2.1 General Principles

Hall and ion thrusters operate by accelerating ions with electromagnetic fields. Within these thrusters, hollow cathodes function to generate plasmas and neutralize the plasma beam created by specific electric propulsion devices. A typical orificed cathode is shown in Figure 1.1. Neutral gas particles are channeled through a hollow cathode into an insert region, where a thermionic insert deposits electrons [10, 14]. Electrons are accelerated by the potential difference between cathode and anode, collide with neutral molecules, and generate a plasma through avalanche breakdown.

Orificed cathodes are refractory tubes with an orifice plate on one end. The orifice plate is electrically connected to a thermionic insert, located just inside the cathode tube. This insert provides a steady stream of electrons via thermionic emission. This emission occurs when the thermal energy of an electron overcomes the work function, ϕ , of a material. This phenomena is governed by the Richardson-Dushman equation:

$$j = A_G T^2 \exp\left(\frac{-e\phi}{k_B T}\right) \quad (1.2.1)$$

Here j is the current density of the emitted electrons, T is the emitter temperature in Kelvin, k_B is the Boltzmann Constant, and A_G is a material constant.

Equation 1.2.1 establishes a monotonically increasing relationship between the electron current density and the emitter temperature. For an emitter to radiate a sufficient number of electrons, the emitter will need a temperature determined by the work function of the material. Several methods are used to achieve this temperature. During startup, a resistive coil heats the cathode for thermionic emission to begin. These electrons ionize the gas in conjunction with an electric field generated by the cathode and anode. During operation, the high energy particles will be expelled through the orifice. This transfers energy to the orifice, which conducts the heat back to the emitter. This allows the cathode to operate in a steady-state condition.

Additionally, the emitter is heated by ion and electron bombardment. The high energy particles will collide with the emitter, transferring energy kinetically. This erodes the emitter, limiting the lifespan of the cathode. Several groups have measured the lifespan of various hollow cathodes [8]. The longest cathode lifespan was recorded by the NASA NEXT Long-Duration Test, where Shastry et al. measured a lifespan of 50,000 hours [19]. Unfortunately, the pool of available data is sparse due to the

time and expense of a life cycle test.

1.2.2 Attachment Length

Presently, there exists no self-contained model to predict the operational life of a hollow cathode. Given the large cost and technical difficulties of operating a cathode to completion, such a model would prove invaluable. In order to create an accurate model, one would need an estimate of the total area over which the temperature-limited thermionic emissions occur.

Thermionic emission creates a region of net negative electric charge near the emitter surface. This *space-charge* impedes the emitted electrons, entirely repelling electrons for large enough currents. Thus, in regions of low plasma density the current density is limited by space-charge. Regions of high-density plasma are capable of accepting greater electron currents. In these regions, the plasma is said to become ‘attached’ to the emitter surface. The length over which this occurs is referred to as the *attachment length*. Here the thermionic emission is no longer limited by the space-charge and plasma density, and instead temperature-driven thermionic emission dominates. A longer attachment length is ideal, as it provides a greater emission current and more efficient use of the thermionic emitter.

Any model predicting the attachment length would need to be supported by experimental results. Determining the attachment length requires axial measurements of the electron density (n_e). This necessitates the design and manufacture of a set of plasma diagnostics to perform these measurements. Section 1.3 will explain probe theory and the techniques used to measure the parameters of a plasma.

1.3 Probe Theory

Calculating plasma parameters requires the use of specialized diagnostics. Understanding how these diagnostics operate requires some prior knowledge on the mechanics of plasmas, of which I will attempt to summarize in this section.

1.3.1 Plasma Sheaths

Plasmas are composed of charged particles. As a result, they are highly sensitive to the presence of any conductor or charged body. When an ungrounded conductor contacts a plasma, the more mobile electrons reach its surface first. This gives the

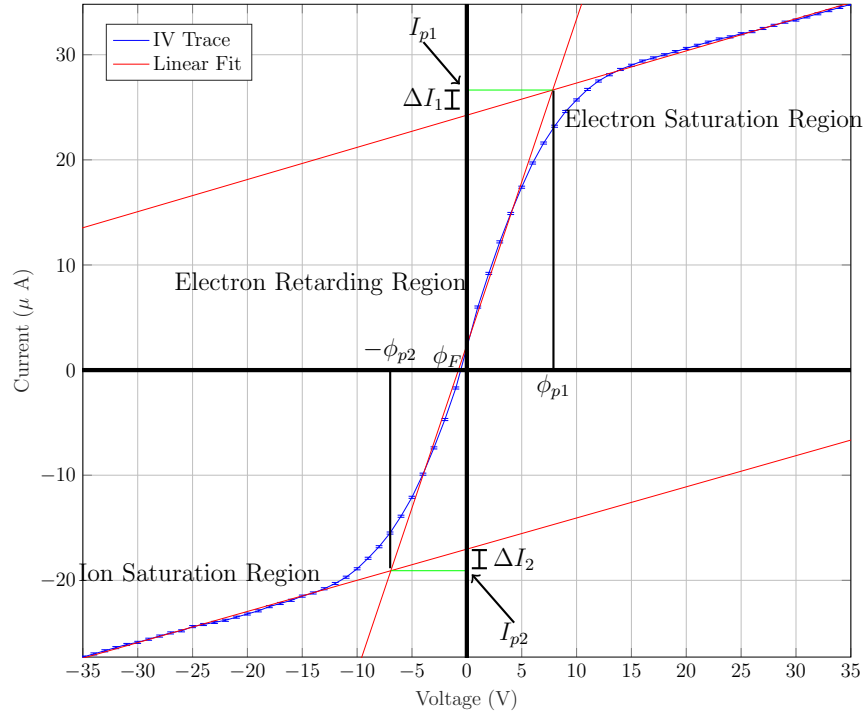


Figure 1.2: Regions and important variables labeled on a probe characteristic

conductor a slightly negative potential and forms a potential sheath that repels low energy electrons. The potential will grow in magnitude until there is no net current between the ions and electrons.

Similarly, a plasma will also react to the presence of a charge. When a charged body is inserted in a plasma, it creates a Debye sheath. Nearby, oppositely charged particles will move towards the body, and will shield distant particles from the effects of the charge. At the Debye length, the effect from the potential is equal to the thermal motion. The sheath effect is negligible beyond this length [11].

Many probes operate on these principles. Through changing the potential on a conductive piece of metal, the amount of charge carriers reaching the probe surface will change. In practice, the potential applied to the probe can be swept across a given range while the resulting current is measured. A typical probe characteristic obtained from this process is shown in Figure 1.2. Sections 1.3.2 and 1.3.3 will detail the functionality of two probe types pertinent to this thesis.

1.3.2 Triple Probes

A Langmuir probe is frequently considered the simplest method of measuring a plasma. A Langmuir probe consists of an electrode supported by an insulating base [5]. Through applying a varying potential to the conductor and measuring the resulting current, the probe characteristic can be constructed, from which the electron temperature (T_e) and electron density (n_e) can be approximated with:

$$T_e = \frac{I_s e}{2k_B} \left[\frac{dI}{dV} \right]_{V=0}^{-1} \approx \frac{e\phi_p}{2k_B} \quad (1.3.1)$$

$$n_e \approx \frac{2}{CA_p e} I_p \frac{I_p - \Delta I}{2I_p - \Delta I} \sqrt{\frac{m_i}{k_B T_e}} \quad (1.3.2)$$

respectively, where ϕ_p is the plasma potential, m_i is the ion mass, A_p is the projected probe area, and C is a geometry constant (.61 for cylindrical probes) [15]. For a single Langmuir probe, the electron saturation current is much higher than the ion saturation current. As a result, any probe biased to collect electrons will receive a large heat flux.

A triple probe is an altered Langmuir probe configuration. As its name suggests, this probe consists of three electrodes immersed in the plasma. Two of the electrodes act as a floating double probe. Biasing the electrodes changes their potential difference, while the mean voltage floats such that it results in zero net current. The third electrode floats, such that its potential would equal the floating potential of the plasma.

The triple probe is used over the single Langmuir probes for two reasons. Firstly, floating probes ensures that the total current would never surpass the ion-saturation current, thus limiting current-based heat flux. Secondly, triple probes also allow measurements to be made with fast time resolution, as measurements may be done without sweeping the potential or rapidly changing the probe bias [11]. By using the potential of the floating electrode, the potential difference of the floating pair, and the current of the floating pair, one is able to calculate the exponential fit to the characteristic shown in Figure 1.2. As a result, the probe may be actuated quickly through the interior of the hollow cathode.

1.3.3 Emissive Probes

Langmuir probes are also able to estimate the plasma potential. For Langmuir probes, it can be approximated as the potential where electron saturation is reached, which corresponds to V_{s1} in Figure 1.2. However, this method is not necessarily reliable and often has a large range of uncertainty.

Emissive probes offers a reliable alternative to determine the plasma potential. Emissive probes continually discharge electrons through thermionic emission. Applying a voltage $V > \phi_p$ prevents electrons from leaving the probe, as they do not have the energy to escape the electrostatic force. If the voltage $V < \phi_p$, electrons can escape [11]. The potential at which the current drops corresponds to the plasma potential. By varying the probe potential and monitoring the current through the probe, I can measure the plasma potential within the hollow cathode.

1.4 Purpose

Within the Electric Propulsion and Plasma Dynamics Laboratory (EPPDyL) of Princeton University, PhD candidates Christopher Wordingham and Pierre-Yves Tournay, under the guidance of Professor Edgar Choueiri, have created a model to estimate the attachment length of a hollow cathode. Their model is based on the assumption that the plasma density decay is governed by charge-exchange-limited diffusion. The approach utilizes a series of models to calculate the electron temperature and density profile within the insert region of the cathode. From these profiles, a value for the attachment length is derived [24].

The members of the EPPDyL are now ready to perform an experiment to verify the accuracy of their model. For this experiment they require a set of diagnostics capable of measuring the plasma parameters within the hollow cathode. Plasma diagnostics frequently must be tailored to each experiment. In addition, few businesses offer plasma diagnostics equipment, and those that do charge prices of multiple thousands of dollars. This means that any diagnostics must be designed and manufactured for each experiment. This thesis will cover the design, manufacture, and implementation of plasma diagnostics, and the preliminary data analysis resulting from said experiment.

This thesis will be structured as follows. The primary constraints and goals are listed and explained, before detailing the primary inspirations for the design. All design decisions are justified, and the motor selection process is summarized. Next,

finite element models are created and analyzed to optimize material selection and cooling. Finally, the system is tested while the cathode is operating. From these tests, the probe measurements are analyzed and compared to those of the EPPDyL model.

Chapter 2

Design Process

The following section details the layout of the experiment, the constraints of the project, and the design parameters that this thesis aims to meet.

2.1 Design Parameters

2.1.1 Experimental Setup

The orificed cathode experiment is conducted in a large fiberglass tank, shown in Figure 2.1. This tank measures 2 meters in diameter, 5 meters in length, and features 8 optical ports from which diagnostic cables and cooling lines can be passed. Two 48 inch diffusion pumps backed by a roots blower and two mechanical pumps enable the tank to maintain an internal pressure of 10^{-5} Torr.

Prior to this thesis, a graphite cathode and steel mounting base were manufactured. These parts provided initial dimensions to size other parts. They are depicted in Figure 2.2. In the hopes of examining a variety of cathode shapes, a modular mounting design was utilized. This allows independent parameters to be varied in future cathodes, while any resulting effects may be measured and recorded. The base features a hexagonal array of holes to mount both the cathode or the diagnostics. The thruster and diagnostics subsystem are located at one end of the fiberglass tank, with roughly half a meter of open space between the mounting base and the tank wall. The base is connected to an aluminum platform inside the tank, from which the rest of the cathode assembly was attached. An image of the experimental setup is shown in Figure 2.2.

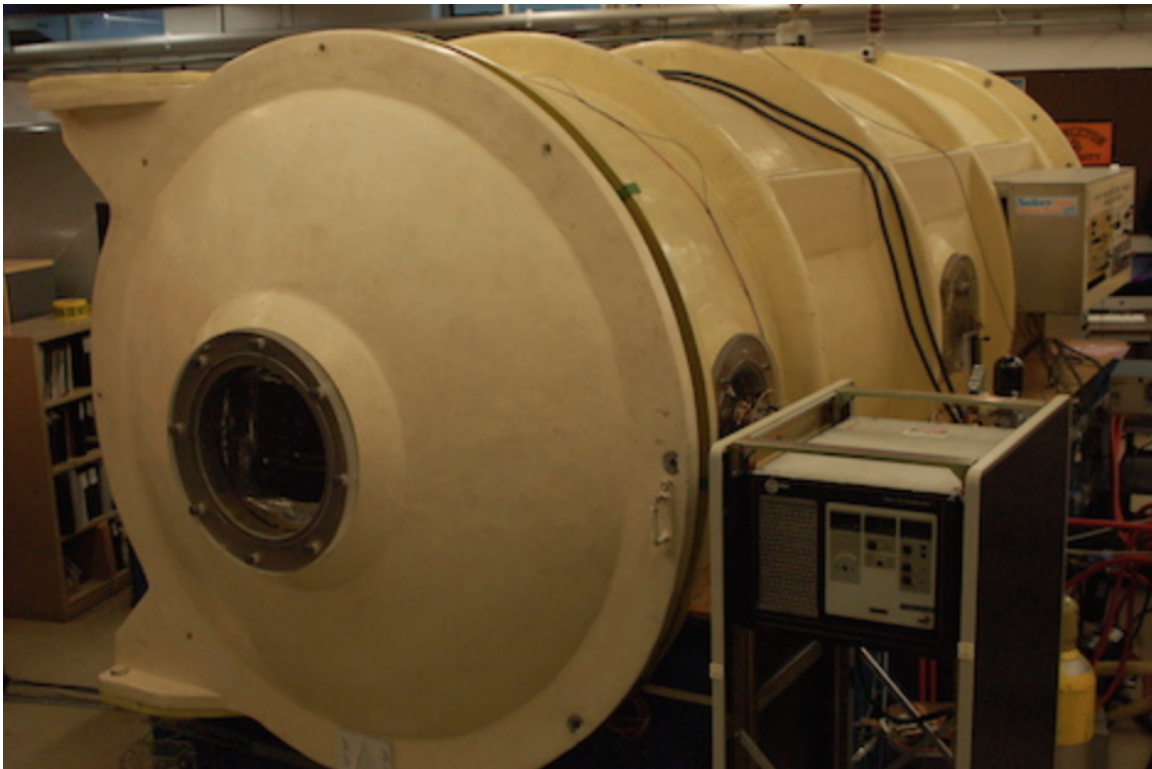


Figure 2.1: Yellow fiberglass tank used in the Pulsed High-Power Performance Facility of the EPPDyL.

During operation, an ionized plasma is created within the orificed hollow cathode. The experiment uses a lanthanum hexaboride (LaB_6) emitter for its easy activation procedure and its resilience to oxygen poisoning. At 1900 K, lanthanum hexaboride emitters are able to create current densities of 10^5 A/m^2 [1]. Current densities of at least this magnitude or higher are required to sustain a plasma within a typical cathode. This generated heat is either radiated to the tank walls or conducted through the cathode, to the base plate and diagnostics subsystem. Several precautionary measures are taken to ensure that the system does not fail due to these thermal loads.

Prolonged contact with the plasma also had the potential to damage the probes. Previous studies conducted by both Siegfried and Wilbur, and Goebel et al., measured electron temperatures and densities within hollow cathodes [21, 9]. The corresponding temperature and densities were measured to be between 1 and 5 eV and up to 10^{21} m^{-3} , respectively. Any probe collecting electrons would receive a large heat flux, which could melt or sputter the probe. Using a thermodynamical simulation, the EPPDyL personnel predicted that a 10 mil tungsten wire has an expected lifetime of around 10 seconds when exposed to these plasma conditions. To ensure that the



(a) The graphite cathode tube

(b) The base plate and clover-shaped anode

Figure 2.2: The graphite cathode and RA253MA steel base plate.

probes are not destroyed, contact with the plasma should be kept below this critical time.

2.1.2 Problem Statement

Based on the experimental setup and requirements, the following lists a summary of the major design constraints for this thesis.

- The diagnostics subsystem must fit within the confines of the existing setup, and can be no longer than 20 inches in length.
- The diagnostics subsystem should be modular. Specifically, the system should be easily attached and removed without having to remove a lot of external connections.
- The structure must maintain structural integrity while the cathode is operating. Materials should not fail due to melting, thermal stresses, or misalignment due to thermal expansion.
- The probes must traverse the entire 8.72 cm (3.43 inch) length of the active region within the hollow cathode. This actuation must occur within 10 seconds in order to avoid thermal damage to the probes.
- The probe position must be calibrated with the signals applied to each of the probes for the entire duration of the actuation.

- Every interface between parts should form a tight gas seal against vacuum. Any leak would misrepresent the final performance of the cathode.
- Every component must be capable of functioning under a vacuum of 10^{-5} Torr.
- The budget for the project is \$2400.

Other factors were taken into consideration, but this list represents the principle factors around which the diagnostics subsystem was designed.

2.2 Overarching Schematic

The following section details the preliminary research and early design decisions. I begin by presenting the primary sources of inspiration, and explaining how these schematics motivated an initial model. I introduce the key concepts behind this model before moving on to the major design decisions in Section 2.3.

2.2.1 Previous Work

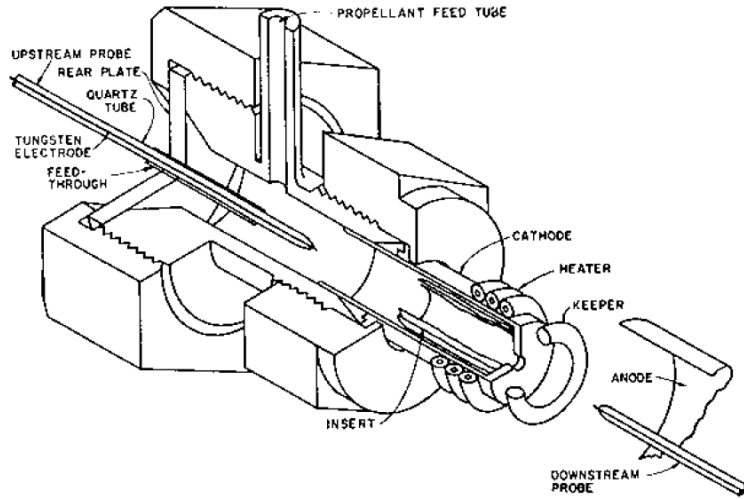


Figure 2.3: The hollow cathode test configuration used by Siegfried and Wilbur.

Before conceptualizing an initial design, preliminary research was conducted on similar plasma diagnostics and hollow cathode experiments. The final design is of the form similar to the test configuration created by Siegfried and Wilbur, shown in Figure 2.3. The probe needed to enter the cathode from the back, and traverse the full length

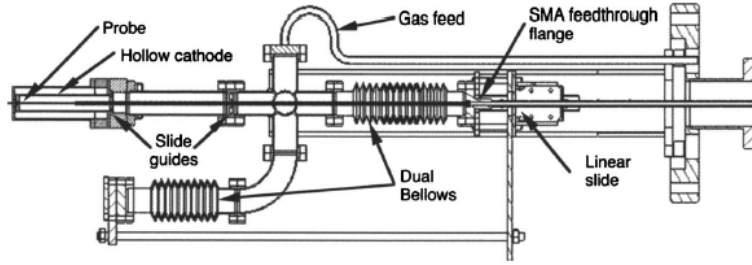


Figure 2.4: Pneumatic scanning probe and dual bellows design created by Goebel et al.

of the cathode without straying significantly from the centerline. Unfortunately, no documentation on the actuation method of this experiment could be found.

Goebel et al. utilized a fast scanning probe to measure the axial plasma parameters within a hollow cathode. The design featured a dual bellows systems. A linear slide actuated the probes and bellows together, keeping the total volume and pressure semi-constant [9]. Several slide guides ensured that all motion would be purely linear.

Despite its promising design, the Goebel design had several problems that made it incompatible with the existing experiment. The cathode studied consisted of a 1.5-cm outer diameter molybdenum tube, in which a .05 cm diameter probe is inserted. By comparison, the cathode to be examined for this thesis measures roughly 3.3 cm in diameter, or 1.3 in. The prices for bellows systems do not scale well with size, and even a small bellows system would have consumed the majority of this thesis’s budget. The actuation method is also challenging. Vacuum-rated linear slides typically have one of two issues. They either do not extend far enough to traverse the full cathode length, or cost roughly three-quarters the budget of this thesis. Alternative cost-effective strategies are required.

2.2.2 Conceptual Approach

In order to maintain constant pressure without using a bellows system, the design from Figure 2.4 was reworked. All mechanical elements responsible for moving the probes are moved within a “diagnostics hangar”. This strategy enables the interior to maintain a constant volume and pressure as the probes are moved. In order to minimize the number of sealed surfaces, the hangar is constructed out of a single large piece of aluminum. The hangar features active cooling, and several ports for wiring to pass through.

I replaced the pneumatic actuator used in Figure 2.4 with a simple motorized leadscrew that transforms rotational motion into translational motion. A plate on each side of the hangar supports the lead-screw and accompanying guiding rod. One of these plates functions as an interface to the base plate for the entire diagnostics subsystem. It also serves as a guide for the probes, in a similar fashion to the slide guides depicted in Figure 2.4. The motor mounts on the other plate.

Since the motor shaft is not sealed, an additional chamber is added to the design. An unsealed shaft could result in a gas leak from the subsystem interior, which would misrepresent the performance of the cathode. This chamber encloses the motor in a sealed volume. A single wiring port is included to transmit electrical signals to the motor.

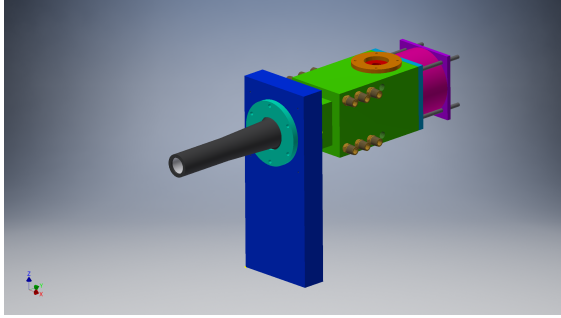
2.3 Structural Design

Autodesk Inventor was the primary tool for modeling and designing the parts for this thesis. This computer-aided-design (CAD) application enabled each of the parts to be modeled and assembled quickly. In addition, the files created were later exported for computer-aided-manufacturing (CAM) techniques. Several renderings of the full CAD assembly are shown in Figure 2.5.

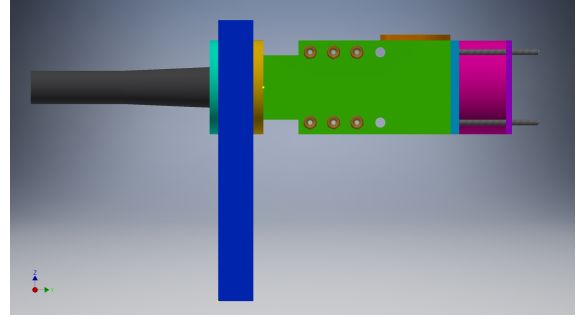
The diagnostics hangar constitutes the main part of the design, and as such, features the most complexity of any part. The hangar was machined from a $4 \times 4 \times 8$ " block of aluminum. For mounting purposes, a $5/8$ " step was removed from each side towards one end. The inner cavity was sized at 2" in diameter, which left enough room for 8 possible cooling ports and a port for external wired connections. This port will be discussed in depth in Section 2.4.2. Numerous blind holes were included on each end for external connections.

An aluminum plate is attached on one end of the hangar. This plate serves as an intermediary between the diagnostics hangar and the motor chamber, as well as a surface on which to mount the motor. A steel plate is connected to the other end of the hangar. It allows the entire diagnostics system to connect with the base plate without excessive disassembly. This plate features a small socket to house a linear bearing and another to house a graphite embedded sleeve bearing. The linear bearing is fastened with obstructing clamp-rings, while the sleeve bearing is press fit.

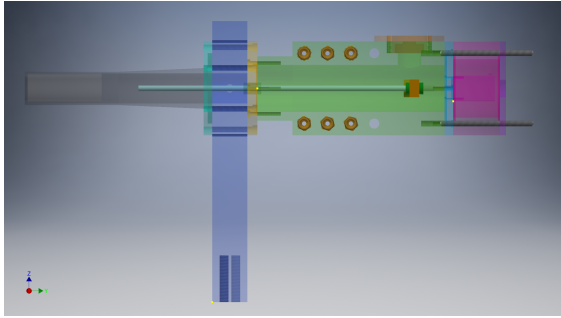
The motor chamber is constructed of a simple annulus wall and square end piece. These pieces were connected to the structure with 3" long $1/4$ - 20 bolts. A hole was drilled in the end plate to allow for an Amphenol connection to transmit the



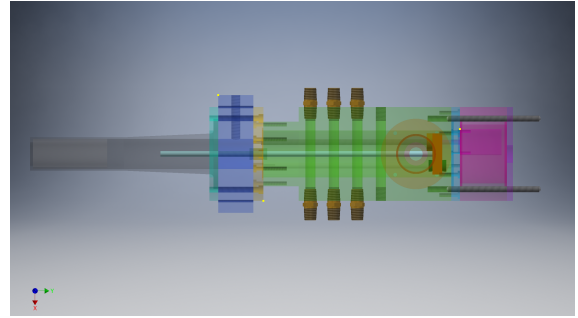
(a) Isometric View



(b) Side View



(c) Transparent Side View



(d) Transparent Top View

Figure 2.5: Multiple views of the assembly for the final design. The cathode tube and base plate are colored in blue and black respectively.

signals for the motor. An Amphenol jam nut receptacle was chosen for its simplicity in connection and for the effective gas seal it provides [2].

A cutaway of the entire assembly is shown in Figure 2.6. Between each pair of parts, a circular o-ring serves to prevent leaks from within the hangar. The o-ring grooves were sized according to the AS568B Standard O-Ring Groove Design [16]. Pieces are fastened such that no screws are located within the diameter of the o-ring. This ensures no gases could escape through the tapped hole. A grafoil gasket is used to prevent leaks between the subsystem and the base plate, as the modular plate temperatures would melt standard o-ring materials.

Several connections are made from the subsystem to the outside of the vacuum chamber. A series of copper coolant lines weave through the NPT coolant ports on the hangar, and connect to the chamber wall. Several wires also need to be fed outside

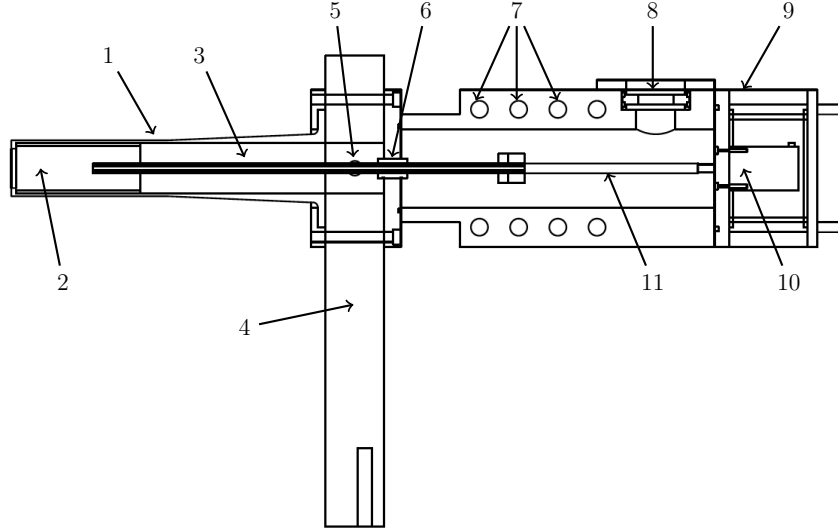


Figure 2.6: Labeled cutaway diagram of the diagnostics subsystem. Cathode is axially symmetric with respect to orifice axis.

| # | Description | # | Description |
|---|----------------|----|----------------|
| 1 | Hollow Cathode | 6 | Slide Guide |
| 2 | Emitter | 7 | Coolant Ports |
| 3 | Probe | 8 | Amphenol Hatch |
| 4 | Base | 9 | Motor Cage |
| 5 | Gas Feed Inlet | 10 | Motor |
| | | 11 | Leadscrew |

Table 2.1: List of Parts for Figure 2.6

the vacuum chamber. These wires are used to either control the motor, or to measure the voltage responses of the probes.

2.3.1 Material Selection

Three primary criteria were used in selecting materials.

1. The materials should survive any expected structural or thermal loads.
2. The chosen materials should minimize the cost of the diagnostics subsystem.
3. The materials should be easily machinable using standard shop equipment.

To ensure materials survivability, an extensive thermal analysis was performed. Chapter 3 covers the thermal modeling processes and the results in greater detail. Aluminum was primarily used for its cost and machinability. In regions of increased

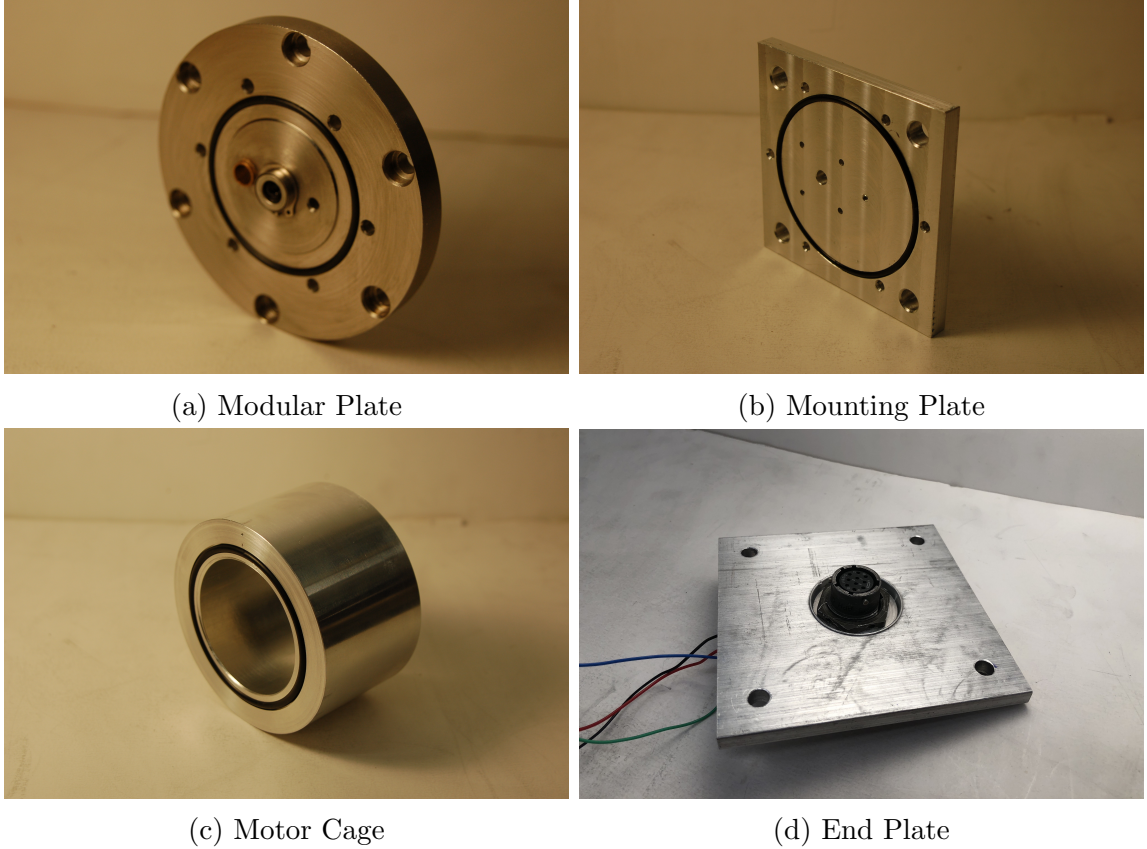


Figure 2.7: Several parts of the diagnostics subsystem. Parts measure 4 inches to a side.

stress or temperatures, aluminum was substituted for steel. Table 2.2 lists every material used for this project.

2.4 Circuitry & Probes

2.4.1 Circuitry

Figure 2.8 depicts the circuit used to manipulate the triple probe. Bob Sorenson designed and built the Langmuir probe driver prior to this thesis.

The Langmuir probe driver features three AD210 isolation amplifiers, one PA341CE high power operational amplifier, and an assortment of additional operational amplifiers, power supplies, and standard circuitry. Part of the circuit is floating with respect to the common ground. This floating section is separated by the isolation op-amps. These amplifiers isolate the high voltage circuitry from the ground, allowing the use of the double probe and improving the safety of the device.

| Part | Material | T_m | σ_{max} |
|-------------------|---------------------|--------|----------------|
| Probe Hangar | 6061 Aluminum | 900 K | 310 MPa |
| Mounting Plate | 6061 Aluminum | 900 K | 310 MPa |
| End Plate | 6061 Aluminum | 900 K | 310 MPa |
| Diagnostics Port | 6061 Aluminum | 900 K | 310 MPa |
| End Plate | 6061 Aluminum | 900 K | 310 MPa |
| Guiding Rod | 6061 Aluminum | 900 K | 310 MPa |
| Motor Cage | 7075 Aluminum | 900 K | 572 MPa |
| Diagnostics Clamp | 7075 Aluminum | 900 K | 572 MPa |
| Modular Plate | 303 Stainless Steel | 1700 K | 690 MPa |
| Probe Slider | 309 Stainless Steel | 1700 K | 586 MPa |

Table 2.2: Part materials for diagnostics subsystem structure.

In the upper left-hand side of Figure 2.8, a signal generator sweeps a voltage 1.5 V peak-to-peak. This signal is given to the first isolation amplifier, which amplifies the signal using a negative feedback loop. The gain is given by

$$G = 1 + \frac{R_1}{R_2}, \quad (2.4.1)$$

where G is the gain, R_1 is the resistor in feedback loop, and R_2 is a grounded resistor. A potentiometer is connected in series with these resistors, allowing the gain to be adjusted. Once amplified, the floating signal is passed to the high power operational amplifier, which is powered by a high voltage power supply capable of providing ± 150 V. Using another negative feedback loop, this amplifier multiplies the gain by 16. This results in a maximum total gain of 100 between the two amplifiers. The output is connected to one electrode of the double probe, which creates an electrical connection through the plasma to the other electrode.

Using the probe return, the two remaining isolation amplifiers track the voltage and current respectively. These amplifiers have unity gain, and simply relay the current and voltage to the grounded circuit. Once transferred the signals are given to buffer amplifiers, which reduces the impedance between circuit sections. From there, the noise is filtered and the values can be measured.

2.4.2 Design & Construction

As discussed in Section 1.3, the attachment length can be approximated through measuring the electron density. To validate the model, the electron temperature was also measured. To perform these measurements, a triple probe and an emissive probe

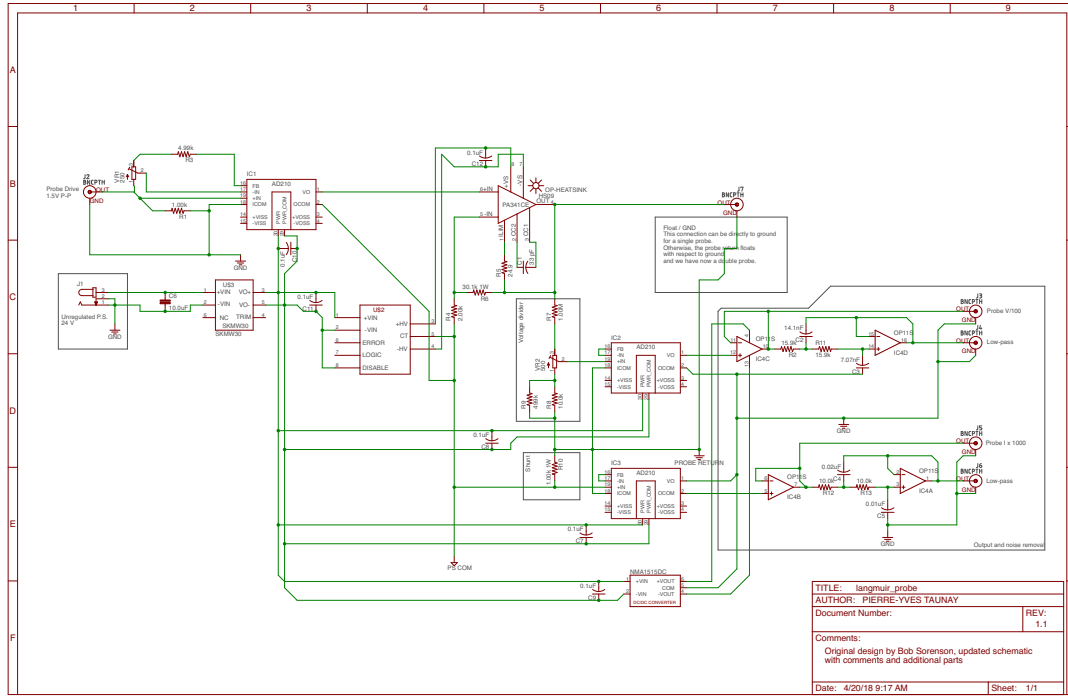


Figure 2.8: Circuit Design to control the triple probe.

were used.

To avoid perturbing the plasma while measuring, the probes size are kept small as compared to the cathode diameter. Materials and part dimensions are determined by their melting temperatures and commercial availability. These values, along with the part dimensions, are indexed in Table 2.3. The probes were comprised of tungsten electrodes encased in a single four-bore Alumina tube. The triple probe occupies three holes, while the emissive probe uses the remaining hole. The Alumina and tungsten are further encased within a molybdenum tube, which shields the wires from electrical interference. The Alumina acts to electrically isolate the electrodes from the shielding and each other.

If it were directly exposed to the plasma, the molybdenum shielding would become an attractive surface for the ions. The ions would attach to the shield, heat it, and sputter it. The shielding is at the cathode potential, meaning the current would travel through the structure towards the cathode. Large enough currents could result in localized melting or deformation of various parts, such as the linear bearing

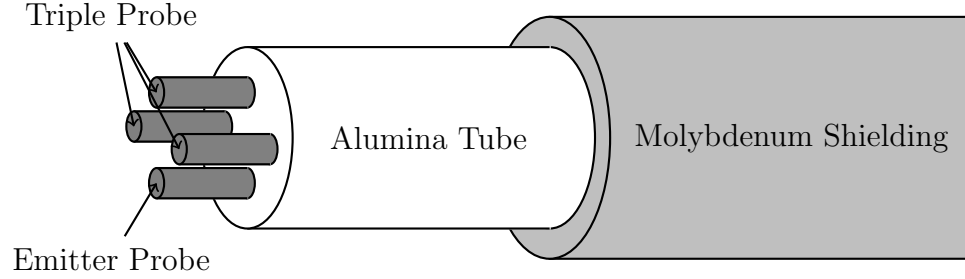


Figure 2.9: Design schematic of the combined Triple - Emitter Probe.

or leadscrew. This should be avoided by applying an insulating layer around the shielding. Boron nitride spray is applied to the outside 5" of the probe. The completed probe is shown in Figure 2.11.

| Part | Dimensions | Melting Temperature |
|-------------------------|--------------------|---------------------|
| Tungsten Wire | OD .03" | 3700 K |
| Molybdenum Tube | .25" OD; .21" ID | 2900 K |
| Alumina Multi-Bore Tube | .188" OD; .031" ID | 2000 K |
| Boron Nitride Spray | N/A | 1900 K |
| OD = Outer Diameter | | ID = Inner Diameter |

Table 2.3: Dimensions and melting temperatures of the probe materials.

The probes are held in a small mount with a set screw. This mount is actuated directly by the lead-screw and held steady by a guiding rod. Shielded coaxial wires transmit the current from the probes to a diagnostics port, depicted in Figure 2.12. To maintain a gas seal, o-rings are placed around the port edges and within the Amphenol connector. Another Amphenol jam nut receptacle is used to prevent leaks through the connector itself. From there, a shielded cable transfers the signals to the optical port of the fiberglass tank. This connector will further transmit the signal to the circuits discussed in Section 2.4.1.

2.5 Motor Selection

2.5.1 Selection Criteria

The motor had to meet four primary requirements:

- The torque is sufficient to overcome the frictional effects in the system.
- The RPM is sufficient to actuate the probe 3.17" and back within 10 seconds.

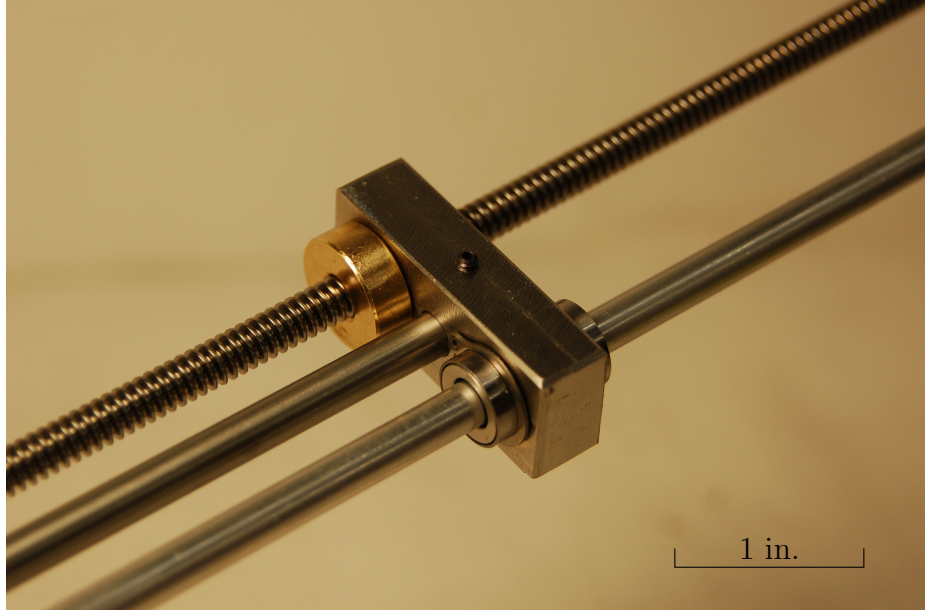


Figure 2.10: Probe slider supported by the leadscrew and guiding rod. See Appendix A.11 for scale.

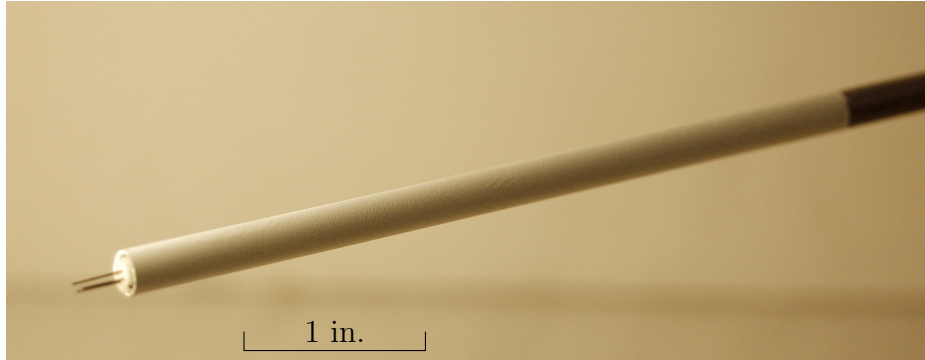


Figure 2.11: Photo of the combined probe.

- The motor must be capable of operating under vacuum conditions of 10^{-5} Torr.
- The absolute position of the motor must be known at all points in time.

The torque τ required to move a mass using a lead-screw can be determined with

$$\tau = \frac{F d_m}{2} \left(\frac{l + \pi \mu d_m}{\pi d_m - \mu l} \right) \quad (2.5.1)$$

where F is the load on the leadscrew, μ is the coefficient of friction, and d_m is the diameter [20]. The small inner diameter of the probe hangar restricts the diameter of the leadscrew to $d_m = 1/4"$. For the given steel lead-screw and a bronze nut, the

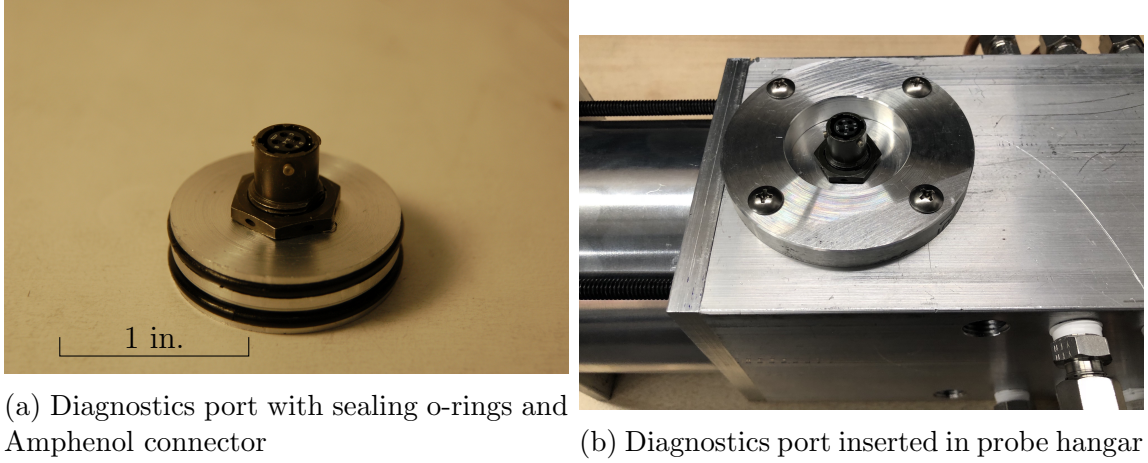


Figure 2.12: The diagnostics port and Amphenol connector. For detailed drawings of the port and clamp, see Appendix A.12 and A.13.

travel distance per turn is $l = 1/16''$ per revolution, and the coefficient of friction is around $\mu = .23$ [20]. F is determined by combining the largest contributions to weight. This resulted in a required torque of 5 oz-in. To confirm this calculation, a rudimentary jig was assembled. A string was wrapped around the leadscrew, and the maximum force was measured with a force gauge. This technique resulted in a required torque of 7.5 oz-in, ensuring that the calculations were on similar orders of magnitude.

The required RPM was determined with,

$$\omega = \frac{x}{tl} \quad (2.5.2)$$

where the total distance is $x = 5''$ and $t = 10$ s. $5''$ is chosen to overshoot the rotational requirements. The minimum angular velocity to meet these criteria using the given lead-screw is 480 RPM. Optimally, the RPM would be around twice this value to include a safety factor of around 2.

The motor selected must be able to meet each of these criteria, and also be capable of operating under vacuum. Vacuum environment poses several problems for motors. For example, brushed motors typically rely on graphite brushes, which require some humidity and oxygen to form a patina layer that maintains an electrical connection and low-friction operation [13]. Brushed motors wear out quickly within a vacuum.

An alternative to brushed motors are stepper motors. A stepper motor is a brushless DC motors that use pulses to increment its rotation position by some number of steps, which corresponds to some specific angle. These motors are convenient, as they

do not require an encoder to determine the absolute position of the motor. Instead one simply needs to signal a certain number of pulses, which will correspond to a given change in angle [7]. However, under high torque stepper motors risk missing steps. This will contribute to the uncertainty in position of the probe.

Despite not having brushes, brushless motors do suffer from other problems in vacuum. The primary issues involve heat dissipation and outgassing. In particular, without convection a motor can only dissipate heat through conduction, which may lead to damage for prolonged operation. Care must be taken so that the region near the motor is properly cooled. Outgassing is when gas is released from materials when placed into a low pressure environment. The grease inside most motors would outgas, and could potentially move from its lubricating position. This would create friction, which would heat up and wear out the motor further. In order to prevent such an even from occurring, vacuum greases and special bearings must be used for vacuum conditions.

2.5.2 Performance Specifications

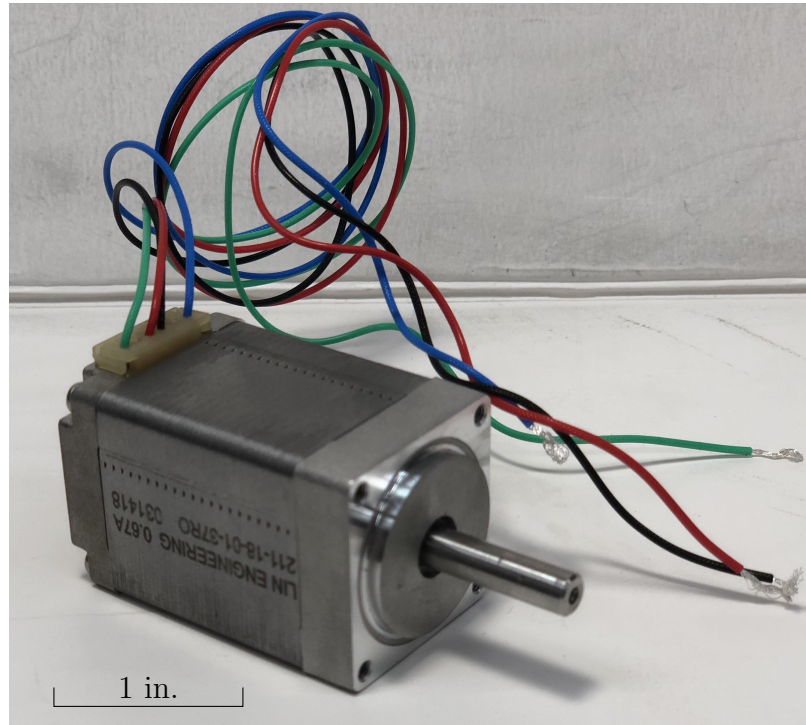


Figure 2.13: The 211-18-01 vacuum rated stepper motor. See Appendix B.1 for scale.

A vacuum-rated DC stepper motor was chosen for the task of rotating the lead-screw. Figure 2.16 depicts the torque curve for this motor. For an expected torque

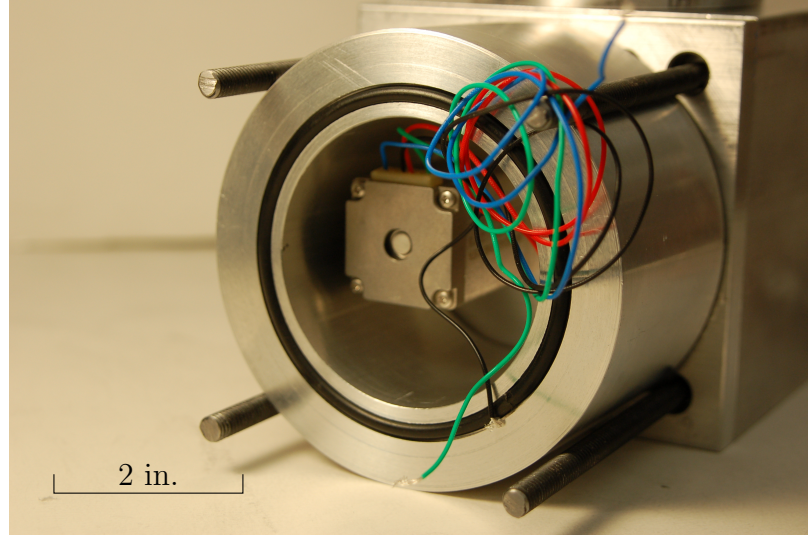


Figure 2.14: Back View

Figure 2.15: The stepper motor mounted to the diagnostics subsystem frame.

of 8 oz-in, the motor is capable of rotating at 1200 RPM. This results in a total time to traverse the cathode to be 8 s, which is well within the requirements. Ideally, the final design would require less torque to overcome friction, allowing a higher RPM. The step angle of the motor is $\theta = 1.8^\circ$. Assuming that the motor will miss no more than n steps per inch, then the error for the probe position can be calculated by,

$$\sigma_x = xnl \frac{\theta}{360^\circ} \quad (2.5.3)$$

which results in an uncertainty of $\sigma_x = 5 \times 10^{-3}$ inches for $n = 1$.

2.5.3 Programming

During the experiment, the motor is remotely controlled via computer. A R256 controller/driver acts as an intermediary between the computer and the stepper motor. The computer communicates with the R256 driver/controller using serial commands. The controller then translates these strings into meaningful pulses to actuate the motor.

For the experiment, I developed a basic program in Labview to control the motor. Figure 2.17 shows the virtual interface and block diagram design. The virtual interface features text boxes to read and write strings, several buttons and switches to toggle various motor functions, and several lists to output position and time measurements.

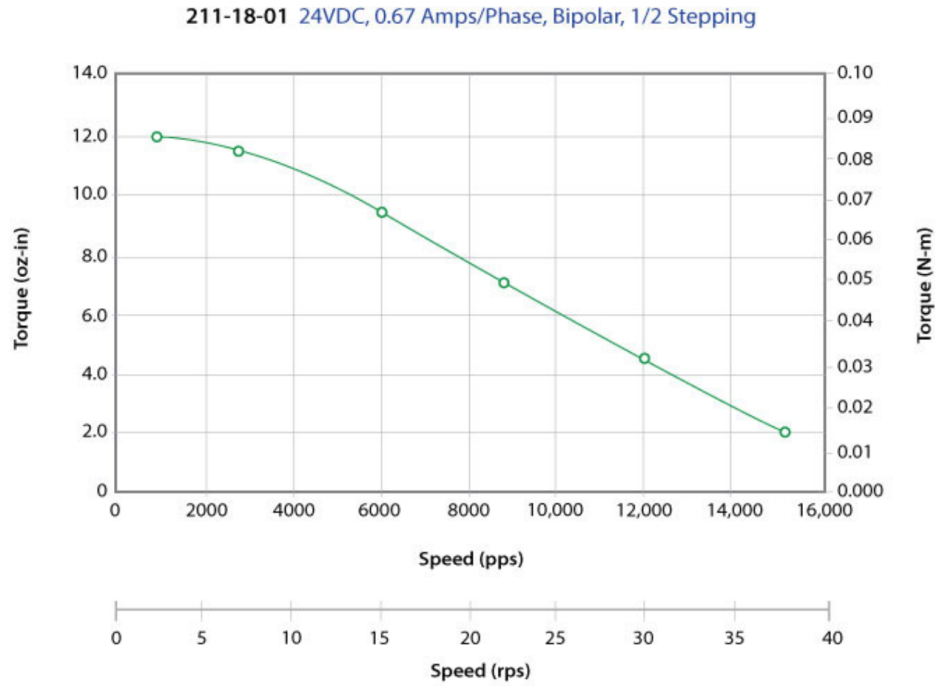


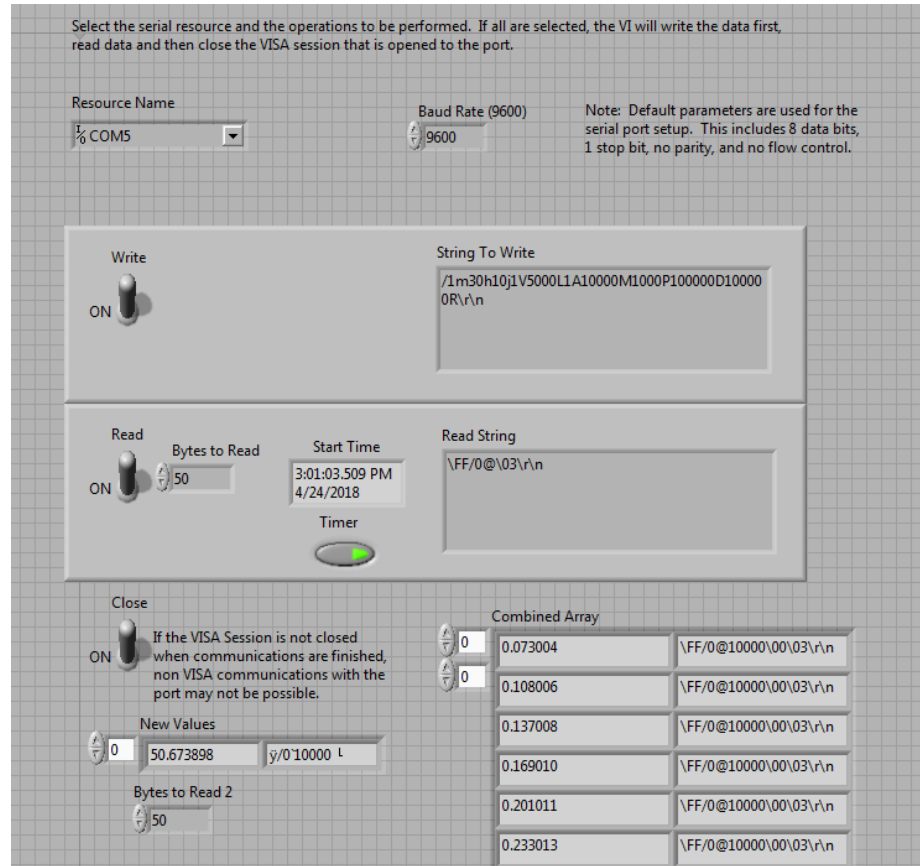
Figure 2.16: Torque Curve for the 211-18-01 vacuum rated stepper motor.

After initializing the serial port and starting time, Labview transmits a written string to the controller. The string used for the experiment is shown below.

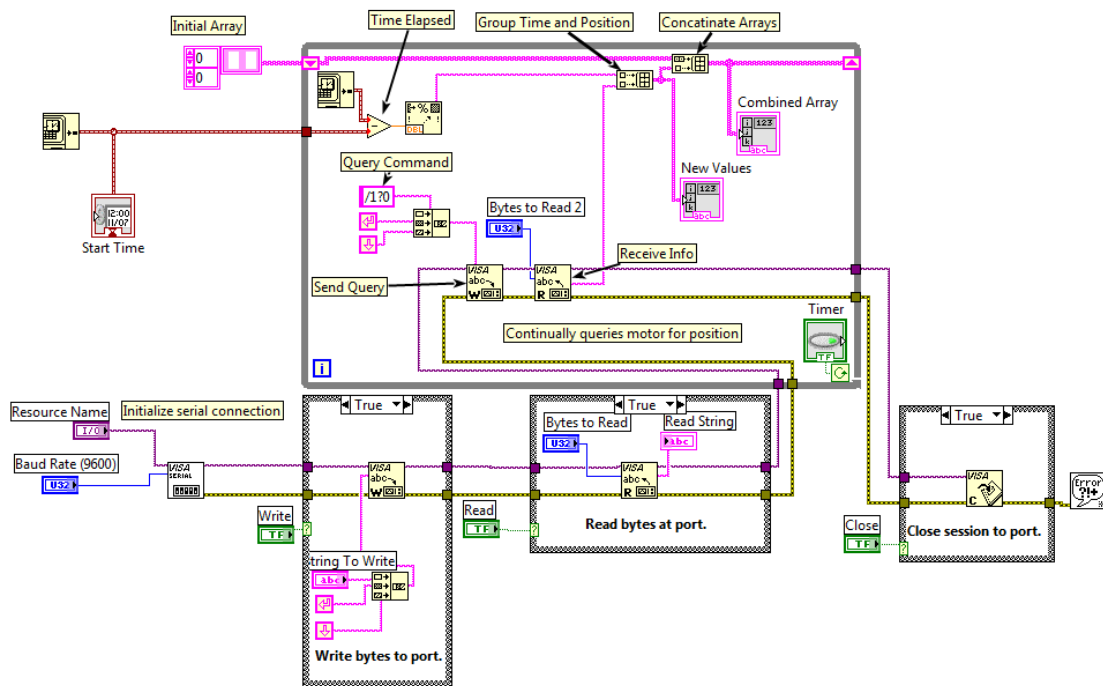
```
/1m30h10j1V5000L10F1z0P11000A0R\r\n
```

This string begins by setting all initial values for current, step size, and more. It moves the motor to its zero position before rotating 11000 steps counter clockwise. This translates to a distance of 3.44", just over the 3.17" length of the emitter. The motor then returns to its original position. Appendix B.1 fully details each of the commands within the string.

After transmitting the string, Labview begins to continuously send positional query commands to the controller using a while loop. The controller responds by returning the absolute position of the stepper motor. The time elapsed is simultaneously computed, and the position and time are appended to a growing array. The time and position measurements are continually updated and displayed on the virtual interface. This allows anyone operating the motor to continuously monitor the position, and terminate the commands if necessary. Once the while loop is disabled, the program closes the serial port and concludes.



(a) Front Panel



(b) Block Diagram

Figure 2.17: Labview schematic to control the stepper motor.

Chapter 3

Thermal Modeling

As discussed in Section 2.1.2, one concern in designing diagnostics is ensuring their survival against the heat fluxes of an active plasma. To justify a given design, extensive thermal and structural analyses are required. Specially the study aimed to determine whether the materials chosen are structurally and thermally viable, as well as the amount of cooling required.

3.1 Initialization

Two finite element simulation softwares were used to generate these analysis. The first, Autodesk Fusion 360, is a combined CAD/CAM software which works in conjunction with the rest of the Autodesk Design Suite. It features basic thermal and structural analysis tools. Using said software, I created early, first-order temperature and structural models to begin preliminary design. Later, I utilized COMSOL Multiphysics simulation software to perform detailed case studies. COMSOL was utilized over Fusion 360, as its physics-based simulation software was both more powerful and provided greater versatility.

3.1.1 Material Properties

During operation, the temperature of the cathode and surrounding parts will vary by several hundred Kelvin. Over this range, the material properties will change significantly. For the analyses performed, the thermal conductivity and heat capacity were modeled to vary with temperature. Values for these parameters were compiled from multiple material studies [17, 18, 4, 3]. Trend lines were constructed for temperatures

| | C_0 | C_1 | C_2 | C_3 | C_4 |
|----------------------|--------|---------|------------|----------|------------|
| Thermal Conductivity | | | | | |
| Aluminum | 233.5 | 0.03938 | -6.97e-05 | – | – |
| Steel | 9.69 | 0.01901 | -2.749e-06 | – | – |
| Heat Capacity | | | | | |
| Aluminum | -61.41 | 7.406 | -0.02023 | 2.43e-05 | -1.023e-08 |
| Steel | 363.1 | 0.3953 | -0.0001379 | – | – |

Table 3.1: Equation constants for the thermal conductivity and heat capacity of the materials.

between room temperature and the melting temperatures of the materials.. Polynomial fits were constructed using a Levenberg-Marquardt algorithm in MATLAB. These fit lines are shown in Figures 3.1 and 3.2, and the equation constants are listed in Tables 3.1. While these fits are not accurate for over all temperatures, for the purposes of this thesis and the temperatures it would encounter they are more than sufficient. The melting temperatures, T_m , and ultimate tensile strengths, σ_{\max} , that are referenced in this section are cataloged in Table 2.2.

$$C_0 + C_1T + C_2T^2 + C_3T^3 + C_4T^4 \quad (3.1.1)$$

3.1.2 Case Studies

Figure 3.3 depicts the results of two preliminary tests. These tests sought to determine whether active cooling and high-temperature, high-stress materials would be required. They included no active cooling in their input parameters. These tests differed by the material chosen for the modular plate; with one test utilizing an aluminum plate, and the other a steel plate.

For boundary conditions, certain surfaces were set at a constant temperature. A value of 2500 K was chosen as a conservative estimate for the emitter surface temperature. This is derived from the Richardson-Dushman equation, where 2500 K is necessary temperature required to maintain a current density of 10^7 A/m² [10]. The aluminum platform supporting the experiment was set at 373 K. This value is based off of previous experiments conducted in EPPDyL, in which the table temperature was monitored.

These results demonstrated that without active cooling, the system would fail. The tests recorded temperatures of over 1000 K, and stresses of over 900 MPa.

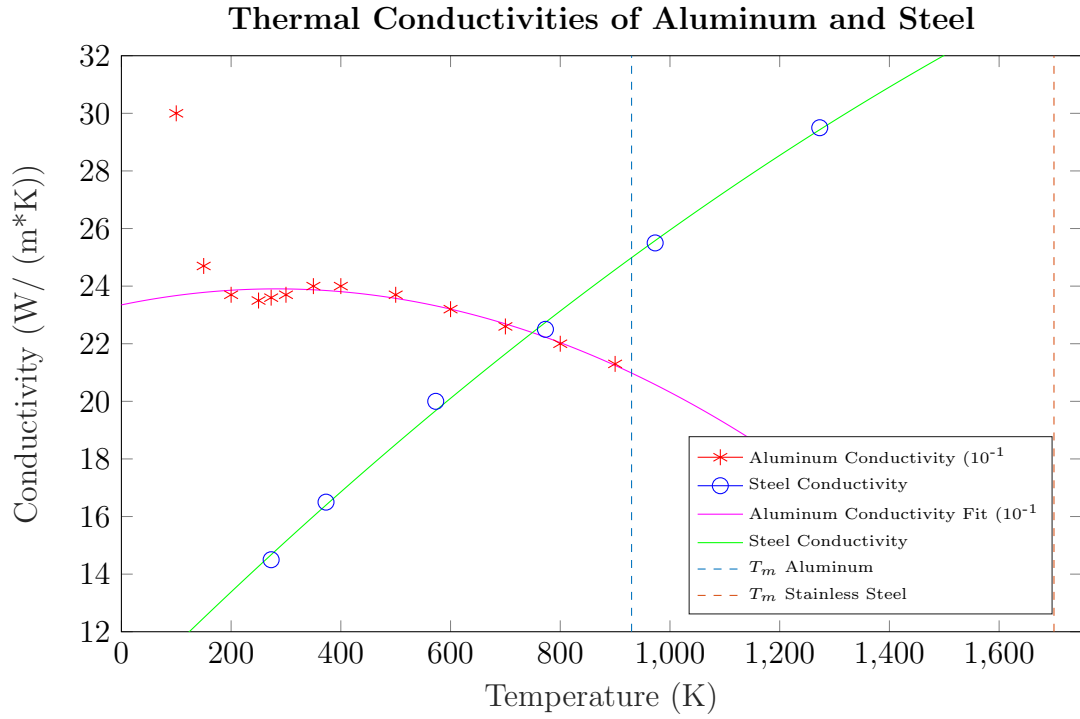


Figure 3.1: Trend lines for the thermal conductivity of aluminum and austenitic steel.

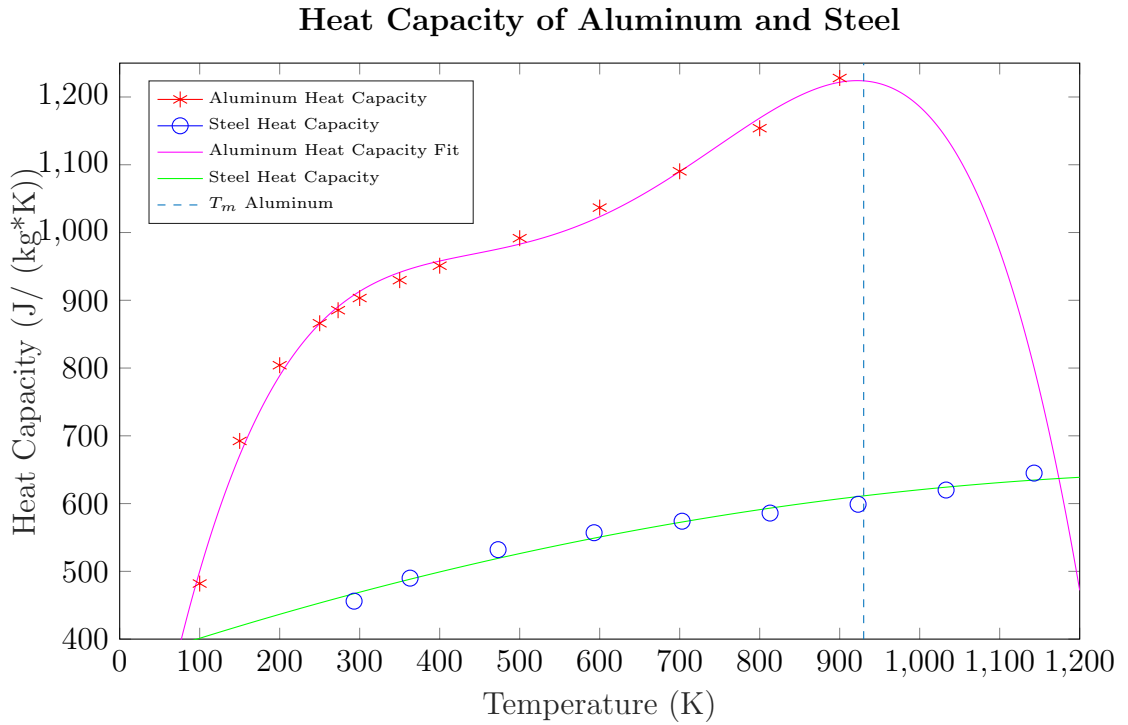


Figure 3.2: Trend lines for the heat capacity of aluminum and austenitic steel.

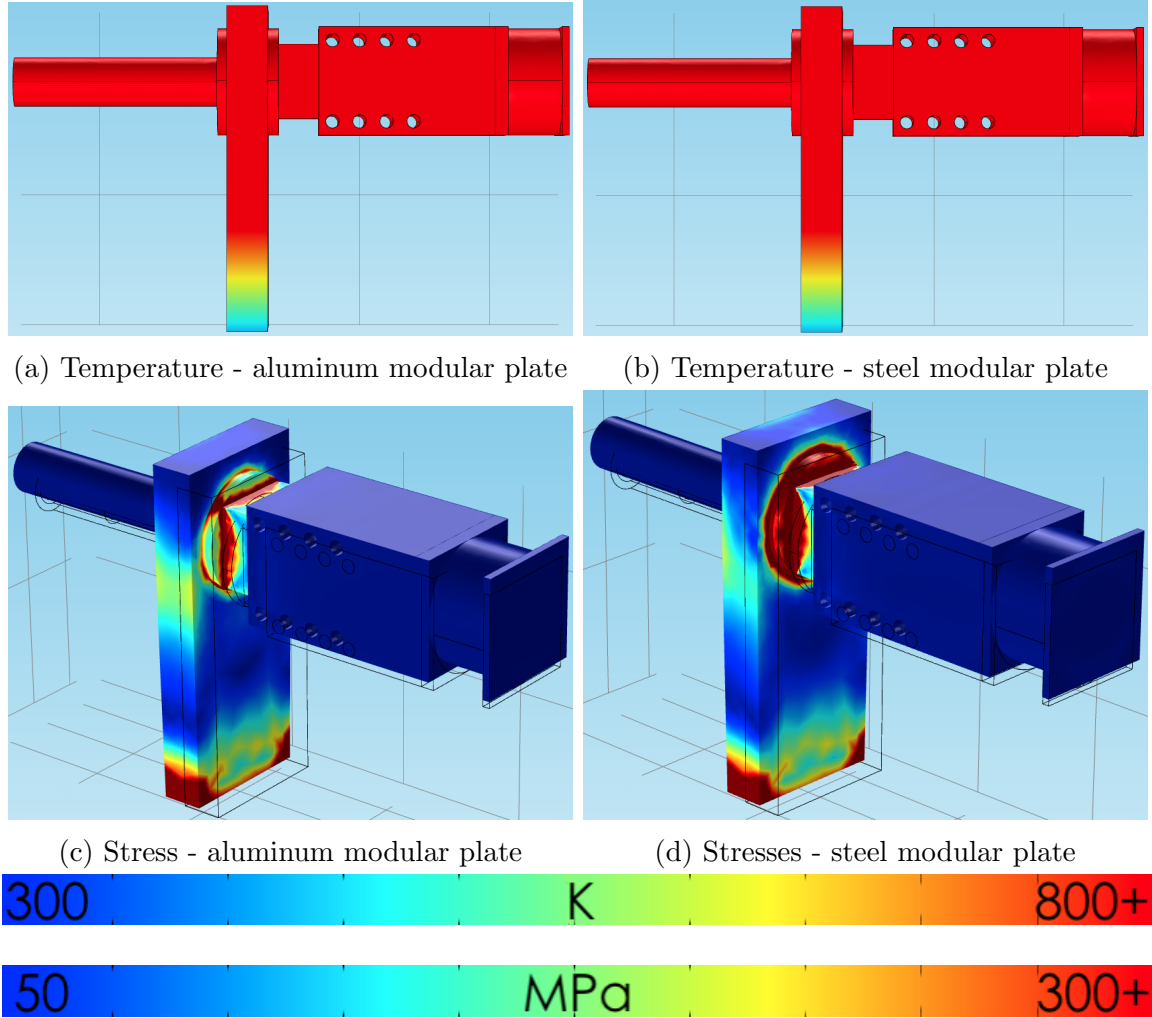


Figure 3.3: Temperature and thermal stress simulations without active cooling.

These temperatures surpass the melting temperatures of aluminum, and near those of steel. The stresses surpass the ultimate tensile strengths of both aluminum and steel. Clearly active cooling would be required. Additionally, the elevated stresses around the modular plate highlighted this region as an area of concern.

Multiple case studies were performed to optimize certain elements of the design. The initial modeling demonstrated that the critical variables were the material of the modular plate, and the number of cooling channels used. Increased coolant channels would improve the survivability, at the drawback of an increased cost. Aluminum and steel were chosen as viable materials, due to their reasonable cost and ease in machining. High temperature steels, such as the RA253MA base plate, were initially considered. These steels were soon found to be unnecessary. Eight studies were

| Study | Modular Plate | Cooling Channels |
|-------|---------------|------------------|
| a | Aluminum | 2 |
| b | Aluminum | 4 |
| c | Aluminum | 6 |
| d | Aluminum | 8 |
| e | Steel | 2 |
| f | Steel | 4 |
| g | Steel | 6 |
| h | Steel | 8 |

Table 3.2: Categorization of the studies performed.

performed to model each variable combination. The relevant studies are categorized in Table 3.2. Additional studies were performed but were not included here for the sake of brevity. Unlisted parts were modeled as aluminum.

3.2 Temperature Analysis

The first analysis performed was a thermal analysis, made in order to ensure each material would not melt by a safety factor of 2. CAD models were imported into Fusion 360, and a thermal analysis was conducted. For this first test, every part of the diagnostics subsystem was modeled as aluminum, and all coolant channels were used. Boundary conditions were approximated using constant surface temperatures. The emitter was set at 2500 K, the and the coolant channels were set at 300 K. This early model did not include the aluminum table boundary condition. The constant surface temperatures assume that the coolant channels are capable of removing all heat from the system, serving as a proof of concept for the active cooling. The results are shown in Figure 3.4. No material surpassed its melting temperature, demonstrated that the conditions were survivable when provided with generous cooling.

The results of Fusion 360 were later confirmed by the COMSOL results, which are shown in Figure 3.5. Simplified CAD models were created within COMSOL using their built-in CAD software. As before, the boundary condition on the cathode emitter was a constant surface temperature of 2500 K, and the aluminum table at 373 K. Unlike the Fusion 360 model, the COMSOL model utilized convective heat transfer to model the water cooling channels. The convective heat transfer coefficient used was $h = 180 \text{ W/m}^2\text{K}$, which was calculated from the Nusselt number for uniform surface temperature for circular pipes,

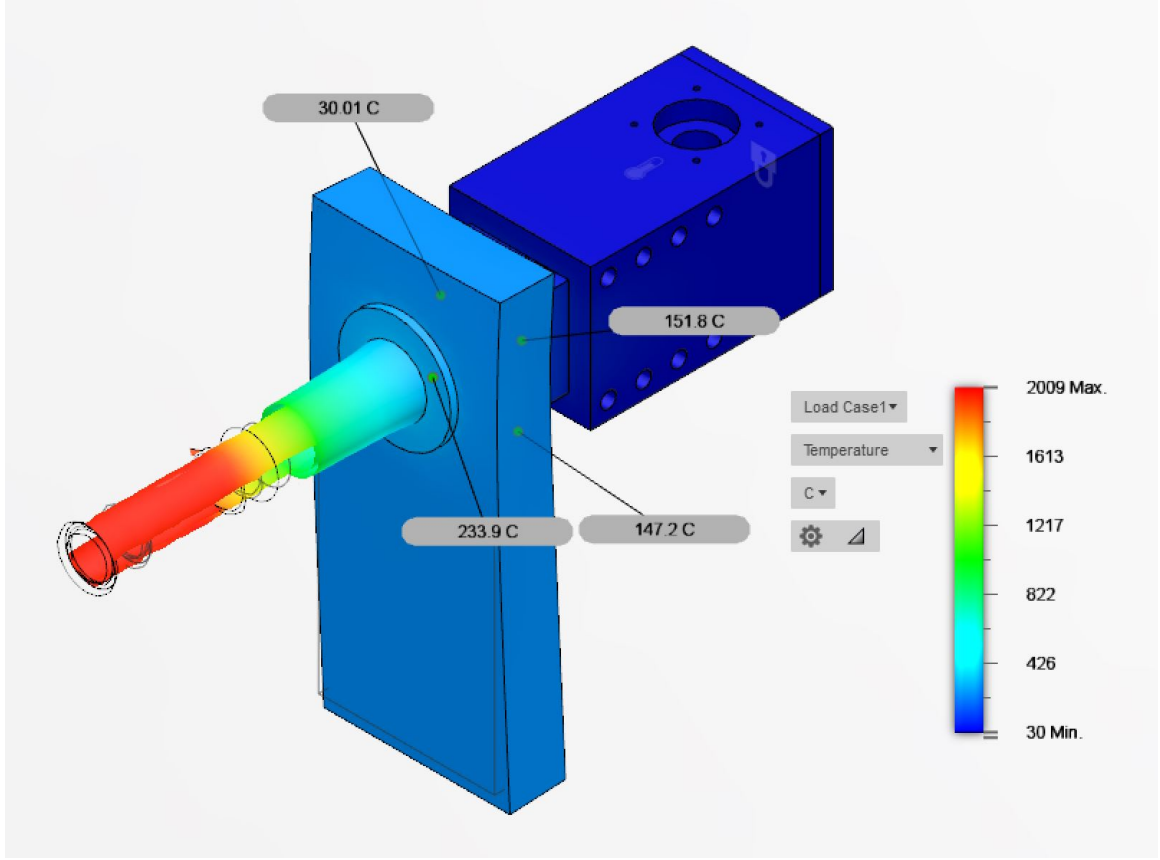


Figure 3.4: Temperature analysis conducted using Autodesk Fusion 360 on an early design model.

$$\text{Nu}_D = \frac{hd}{k} = 3.66 \quad (3.2.1)$$

where D is the diameter of the channel, and k is the thermal conductivity of water [12].

Radiative cooling was ignored for all simulations. However, that is not to say that it is negligible in the context of the experiment. Given the temperatures of the emitter, and by extent the surrounding cathode, the radiative heat fluxes could be considerable. These fluxes were ignored to create a conservative estimate on the temperature profile of the diagnostics subsystem. This ensures that any resulting analysis survive the thermal loads by a generous safety margin.

Increasing the number of cooling channels decreased the overall temperature, with later studies exhibiting diminishing returns. Being closest to the cathode, the modular plate and the probe hangar experienced the greatest heat fluxes. The maximum temperatures for these parts are graphed in Figure 3.6. Studies (a) and (e) demon-

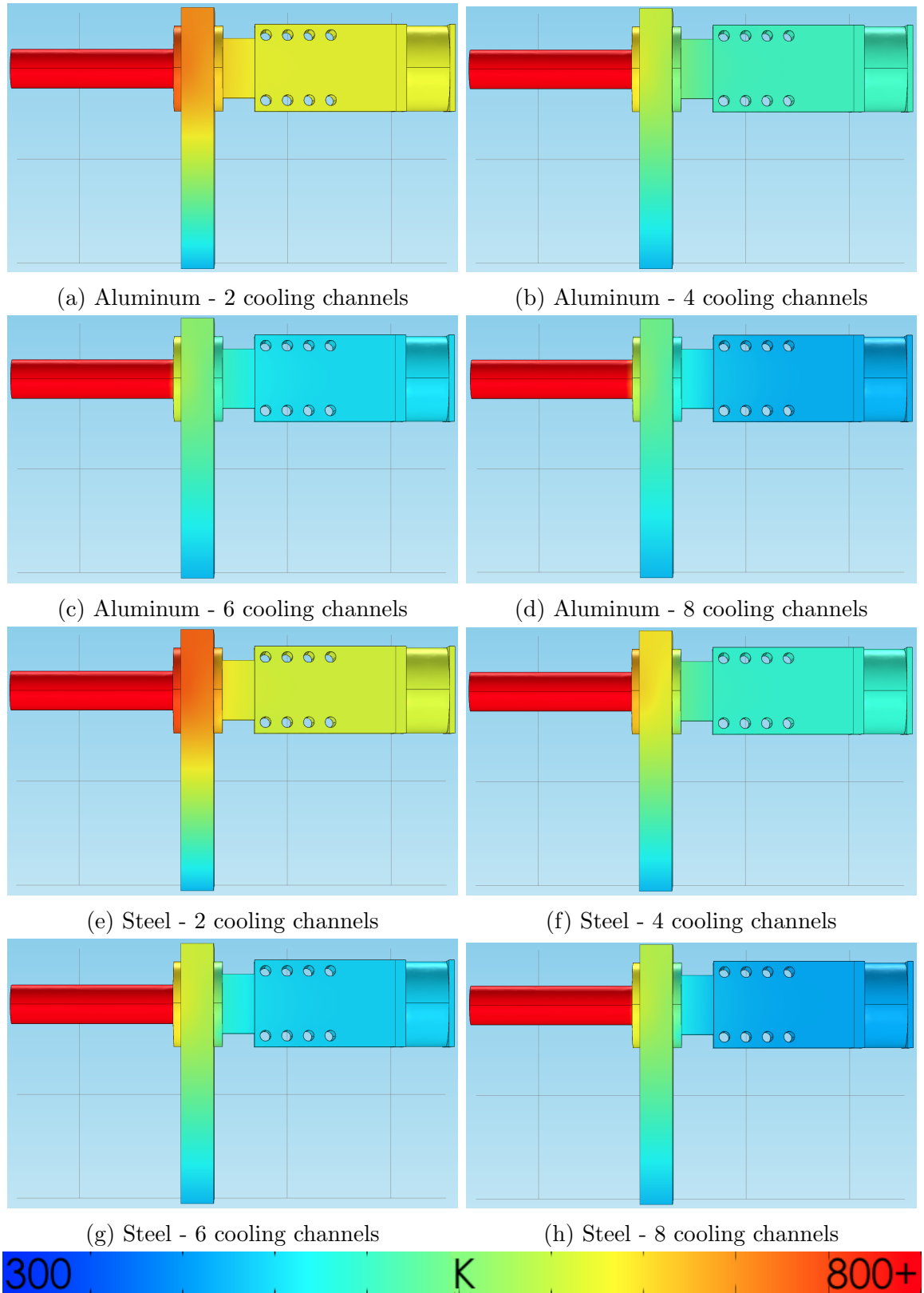


Figure 3.5: Thermal models of each of the studies performed. Color scale is capped at 800 K to show variance in temperature.

strated that with only 2 cooling channels, the design was capable of withstanding the temperature. Their estimated temperatures were between 650 and 700 K. While under T_m , these parts would result in significant structural weakening. More cooling channels improved the design, with studies (d), (g), and (h) falling below T_m by a safety factor of 2. After 6 cooling channels, adding more resulted in insufficient benefits, with temperatures differing by only 20 K between 6 and 8 cooling channels. Ultimately I decided to use 6 coolant channels, as this kept the cost to a minimum.

The choice of material for the modular plate did not significantly change the temperature profiles. However, the proximity to the plasma and cathode convinced me to make the modular plate out of steel. This had greater structural benefits pertaining to the thermal stresses, which will be discussed in Section 3.3. Any further use of steel would increase the cost and machining difficulty.

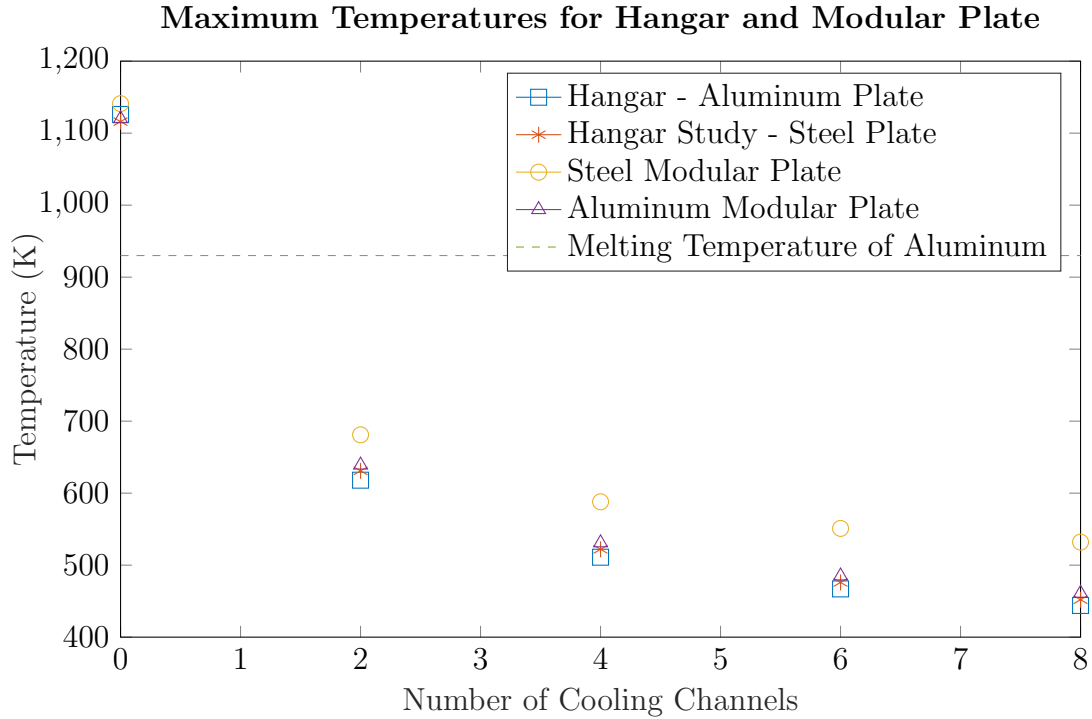


Figure 3.6: Maximum temperatures attained in the modular plate and probe hangar.

3.3 Stress Analysis

Another concern was that the thermal expansion at the part interfaces would create stresses on the parts and fasteners. The materials have differing coefficients of thermal expansion, α_L , which creates a strain on the material when heated. Additionally, the

design had to survive any mechanical stresses caused by gravity. The design was cantilevered from the back of the base plate, focusing the torque on the modular plate, and to a lesser extent, the probe hangar.

Regular mechanical simulations were performed using Fusion 360. While performing thermal stress analysis using Fusion 360, the extreme temperatures created irregular stress patterns within several of the parts. It is believed that this was brought about by irregular heat fluxes between the meshes of separate parts. No fix could be found within Fusion 360. For the thermal stress analyses, COMSOL Multiphysics was used instead.

3.3.1 Thermal Stresses

The version of COMSOL that I had access to did not have a thermal stress analysis package, unlike Fusion 360. In order to perform such a test, I altered the governing equations in the thermal analysis package by appending the linear thermal expansion equations,

$$\frac{\Delta L}{L} = 3\alpha_L \Delta T \quad (3.3.1)$$

where L is the length of the material, and α_L is the coefficient of linear thermal expansion. As a result of this alteration, local maximum stresses could not be determined using the standard integration functions. Fortunately, all global maximums were located within the modular plate.

The simulations were conducted concurrently with the thermal analysis simulations, and the results are shown in Figure 3.7. Similar to the thermal analysis, increased cooling improved the design significantly before reaching diminishing returns. However, the material choice played a larger role in the stress analysis. As depicted in Figure 3.8, an aluminum modular plate would exceed its ultimate tensile strength regardless of the number of cooling channels. A steel mounting plate would remain under σ_{\max} with a considerable safety margin for studies (g) and (h). This is explained by the coefficient of thermal expansion of the modular plate, which is similar to the coefficient of the RA253MA steel base plate. The two expand at similar rates, minimizing the stresses. The steel plate also acts as a thermal buffer so that the temperature difference between it and the probe hangar are closer. Ultimately, it was determined that a steel modular plate would be required.

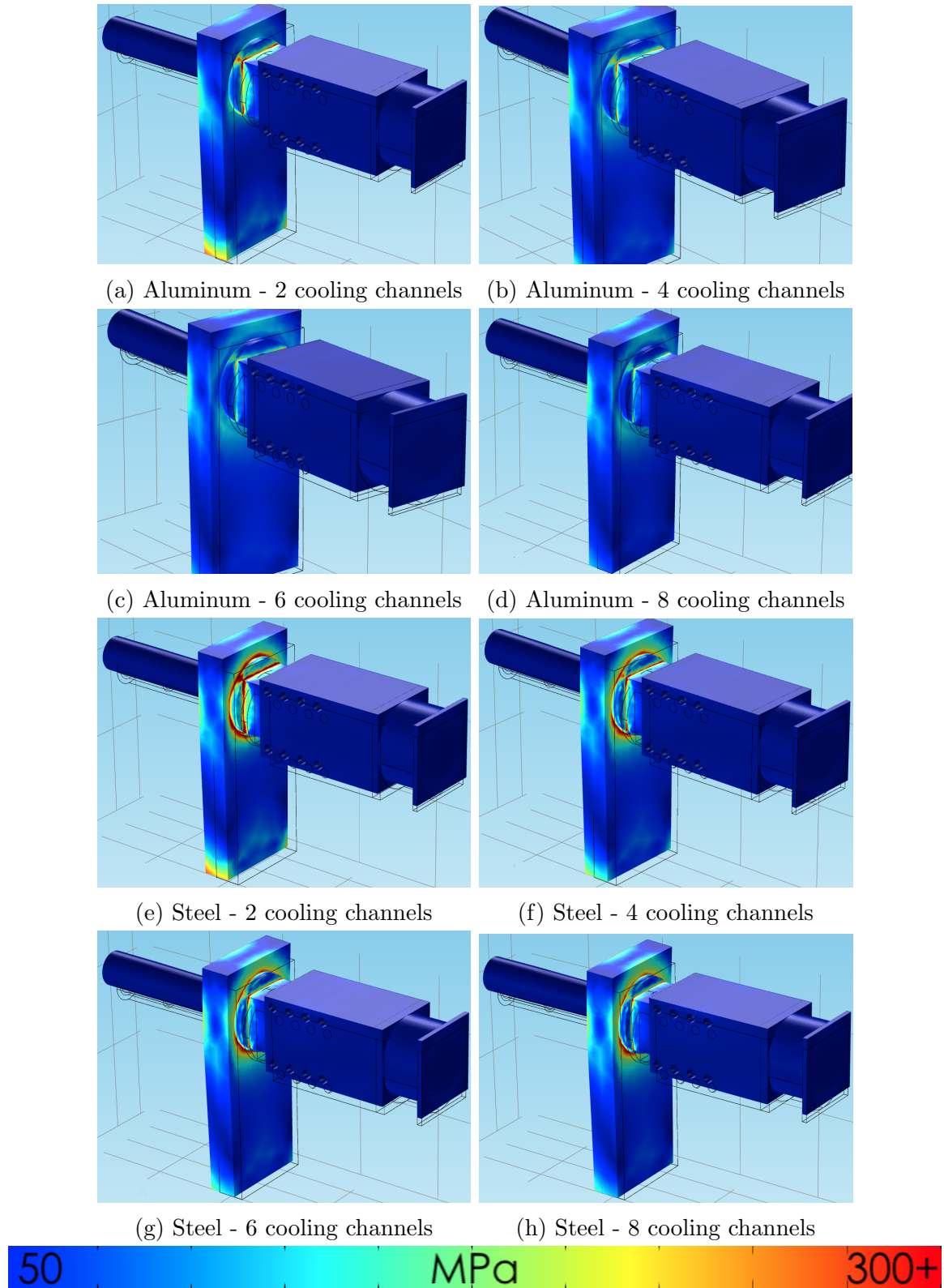


Figure 3.7: Thermal stress models of each of the studies performed. Stresses capped at 300 MPa to show variance across model

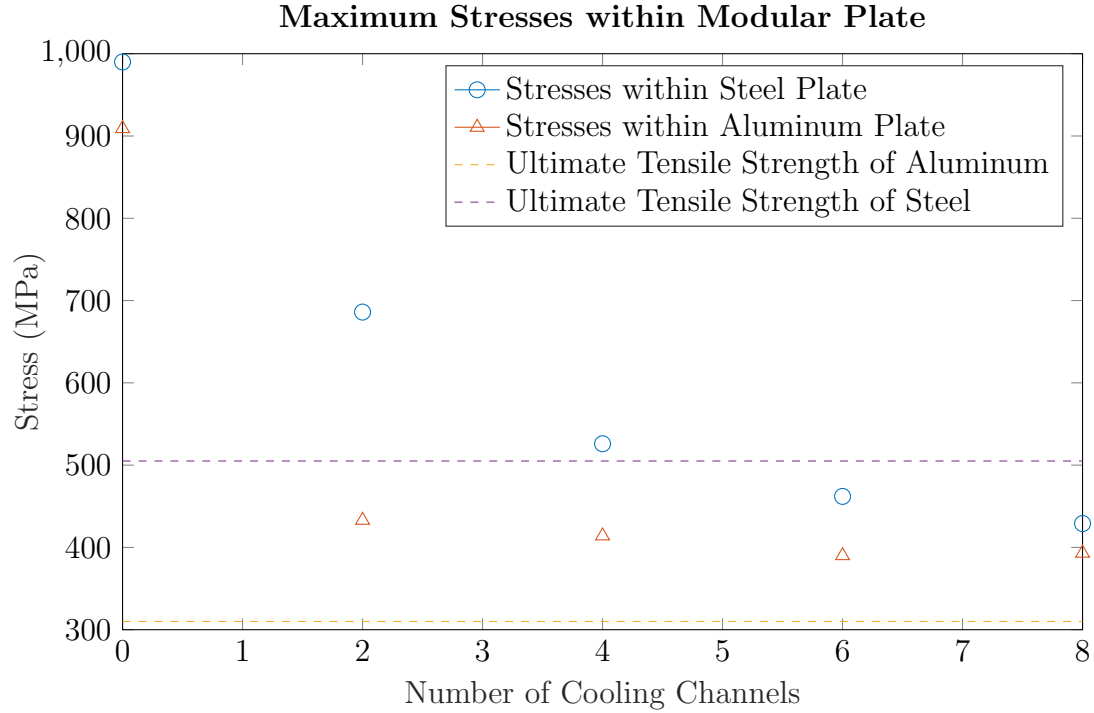


Figure 3.8: Maximum stresses attained in the modular plate.

3.3.2 Mechanical Stresses

The gravitational stresses were calculated using Fusion 360's built in gravitational forces model. This model computes the center of gravity and mass of each of the parts, and applied the gravitational forces accordingly. The results of these models are showcased in Figure 3.9. The maximum stresses due to gravity were around 0.19 MPa – three orders of magnitude lower than those discussed in Section 3.3.1. With such a discrepancy in magnitude, the mechanical stresses were considered negligible. It was also concluded that the subsystem would require no further structural support to hold its weight.

3.4 Summary

The diagnostics subsystem was thermally modeled to determine the appropriate materials, the quantity of active cooling, and the overall feasibility of the design. First, a thermal analysis was performed to ensure that each material would not melt when subjected to thermal loads. Stress analyses were then conducted to ensure that the subsystem would not only survive the stresses due to thermal loads, but also due

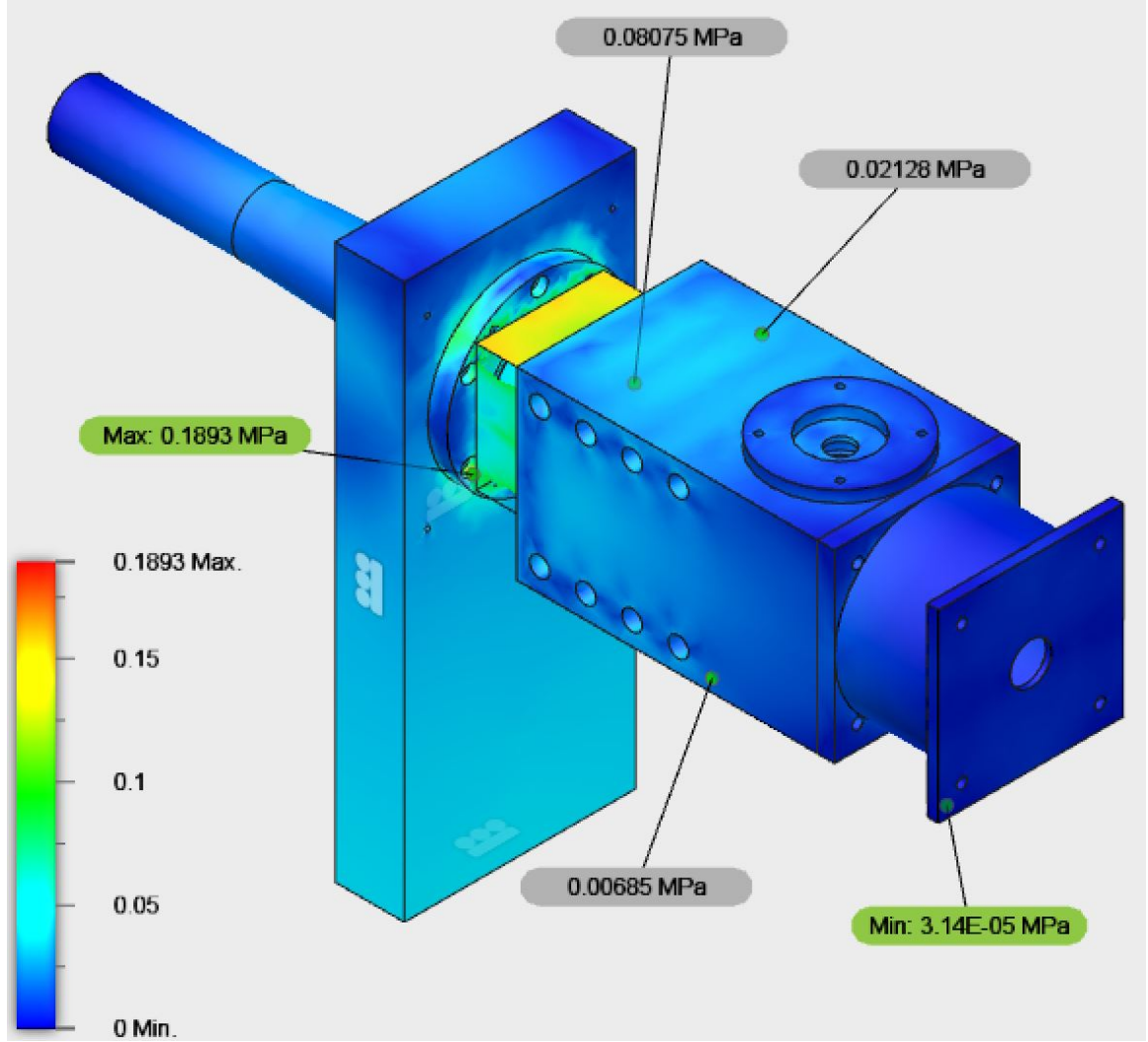


Figure 3.9: Mechanical stresses of the system due to gravity.

to its own weight. Eight situations were studied for each type of simulation. From these studies, it was determined that for more than six cooling channels, the marginal benefits become negligible. However, more could be used for assurance. It was also determined that gravitational forces are negligible when compared to thermal stresses. To keep the maximum temperatures and stresses below their respective melting temperatures and ultimate tensile strengths, the strategy cataloged in Study (g) should be used. This strategy consists of 6 cooling channels and a steel modular plate. Additional holes will be included in the final probe hangar design as a provision if 8 channels are deemed necessary after this thesis.

Chapter 4

Results and Discussion

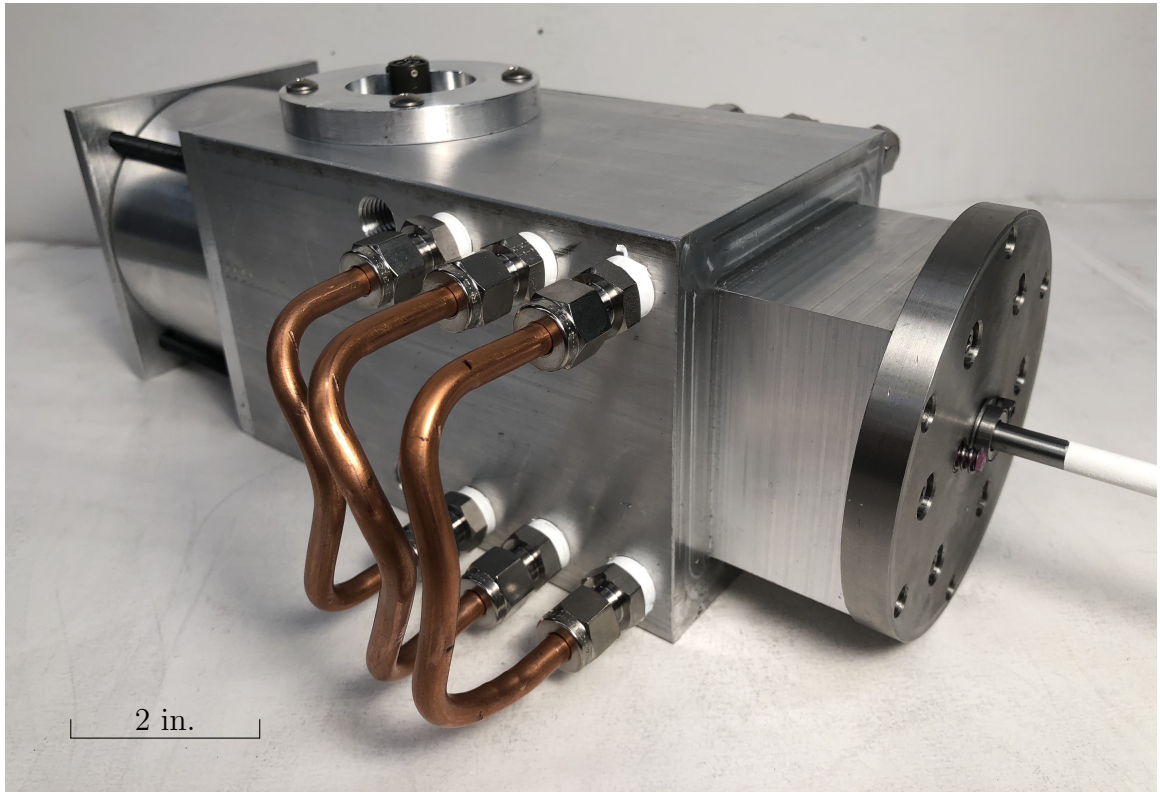
This closing chapter serves to highlight several aspects of the final design and explain the results of a demonstrative assessment. This assessment confirmed that the diagnostics subsystem would perform under experimental conditions. The design and experiment are discussed before the conclusion.

4.1 Final Design

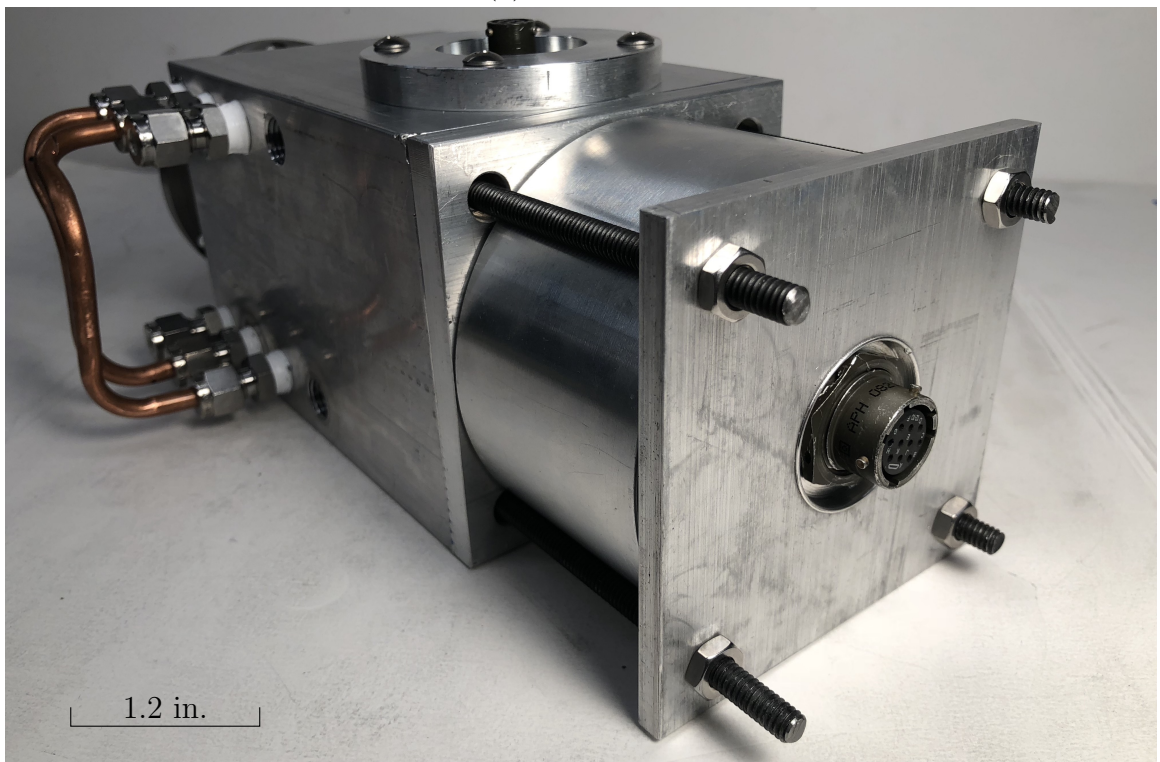
Figure 4.1 depicts the final manufactured diagnostics subsystem. The system measures 11.75 inches in length, and weighs approximately 13 pounds. Following assembly, the subsystem underwent a series of ‘dry tests’ to ensure functionality.

The primary tests performed ensure that the motor is capable of actuating the probe to the desired specifications. Once built, the probe slider had a range of 12000 steps, which translated to a travel distance of 3.75”. The motor is capable of rotating at 5000 steps/s with an acceleration of 10 steps/s². Calculations performed in Section 2.5.2 predicted that for a conservative estimate of 8 oz-in of torque the motor would be capable of rotating at 1200 RPM, or 4000 steps/s. This indicates that the torque in the system is approximately 6.4 oz-in, just short of the 5 oz-in predicted by Equation 2.5.1. The extra friction is likely accounted for in the motion of the linear bearings, which were not previously taken into consideration.

At a velocity of 5000 steps/s, the probe was actuated the full 3.75” and back in 5 seconds. These times were calculated using the Labview absolute time measurements. Figure 4.2 shows a calibration curve created from the Labview position measurements. This calibration curve demonstrates that the position increases linearly with time,



(a) Front View



(b) Back View

Figure 4.1: The final diagnostics subsystem design.

with the exception of a brief initial acceleration.

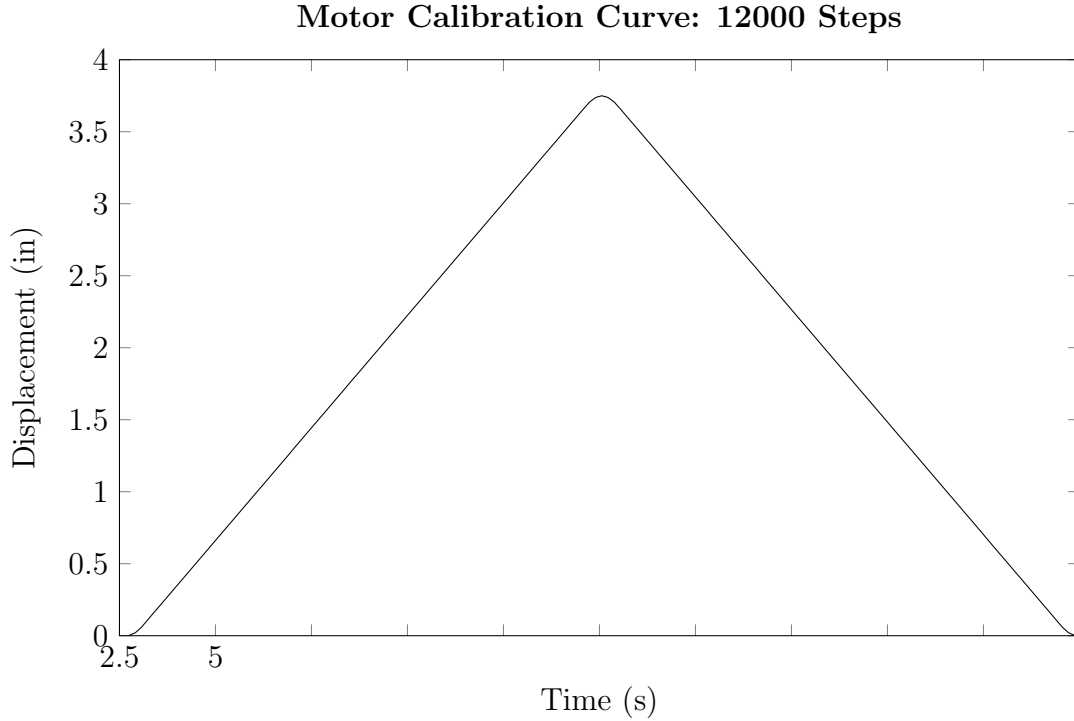


Figure 4.2: Calibration curve for 12000 steps.

During the experiment, the probe did not traverse the entire range of 12000 steps. At this number, the probe would extend to 9 inches and crash into the cathode orifice plate. A mechanical stopper was added to prevent accidental over-extension. In addition, the step count was reduced to 11000 steps, which corresponds to 3.44”.

In addition to the motor testing, each of the external connections were examined. Electrical continuity was checked for each of the probe and motor cables. The cooling channels were attached and inspected for leaks. Plastic tubing connected the diagnostics assembly to the tank exterior, where the flow rate was measured. All leaks were located and plugged. The flow rate to the diagnostics was measured at .34 gal/min.

After examining the diagnostics assembly, the remainder of the cathode system was built and tested. Afterwards, the fiberglass tank was pumped down to a pressure of 10^{-5} Torr for the assessment to begin.

4.2 Experimental Results

The objective of this thesis was to create a system of diagnostics capable of measuring the plasma parameters within an orificed hollow cathode. From these plasma

parameters, the cathode attachment length would be determined, which would be juxtaposed against the EPPDyL model. A final experiment was conducted in order to test the diagnostics. Following the manufacture, assembly, and dry testing, the design was incorporated into the experimental setup within the fiberglass tank. The experiment is imaged in Figure 4.3.

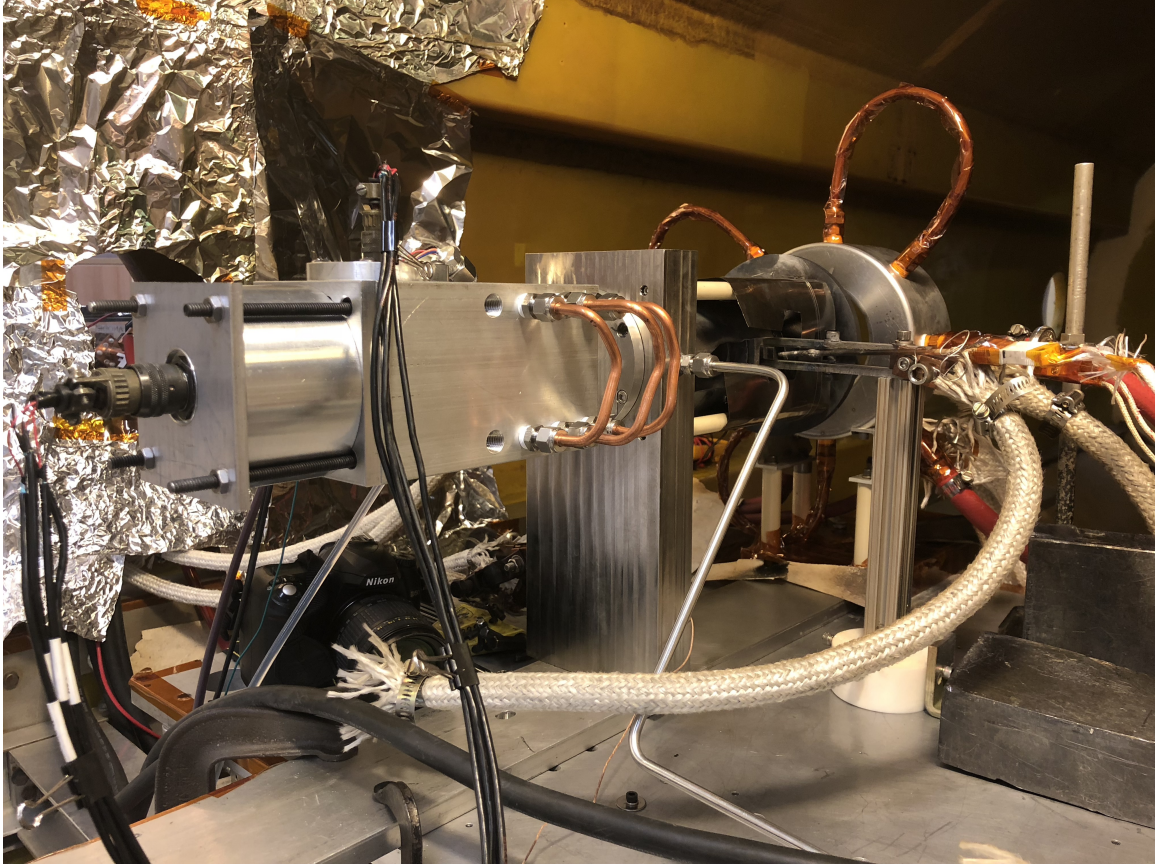


Figure 4.3: The final design implemented into the experimental setup.

Due to a last minute hardware failure, I was unable to take sweeping measurements using the Langmuir probe driver. Furthermore, while the cathode was able to generate a plasma, it was unable to reach steady-state conditions.

The orificed hollow cathode created an argon gas plasma with currents of up to 25 A. The total experiment lasted for approximately 20 minutes. During this time the maximum cathode temperature measured was 1577 K, and the front of the base plate was measured to be 394 K. By comparison, the thermal analysis predicted the base plate temperature to be around 577 K. One reason for this discrepancy is radiation. Radiation is significant at elevated temperatures, and would result in an outward heat flux for the cathode. It is also likely that the cathode did not reach the 2500 K



Figure 4.4: The cathode in operation within the fiberglass tank.

assumed in the finite element model.

As shown in Figure 4.5, the diagnostics assembly appears unaffected by the heat fluxes of the experiment. The greatest heat fluxes occur while the heater is initializing the cathode. Despite not reaching steady-state cathode operation, the system would not fail if it were.

The motor was also tested under experimental conditions. A series of maneuvers were performed, which actuated the probe back and forth. Each maneuver was successful, and the motor continued to operate following the experiment.

4.3 Discussion

4.3.1 Future Work

The design meets each of constraints outlined in the Section 2.1.2. However, while assembling the final design, several issues became apparent. These problems are

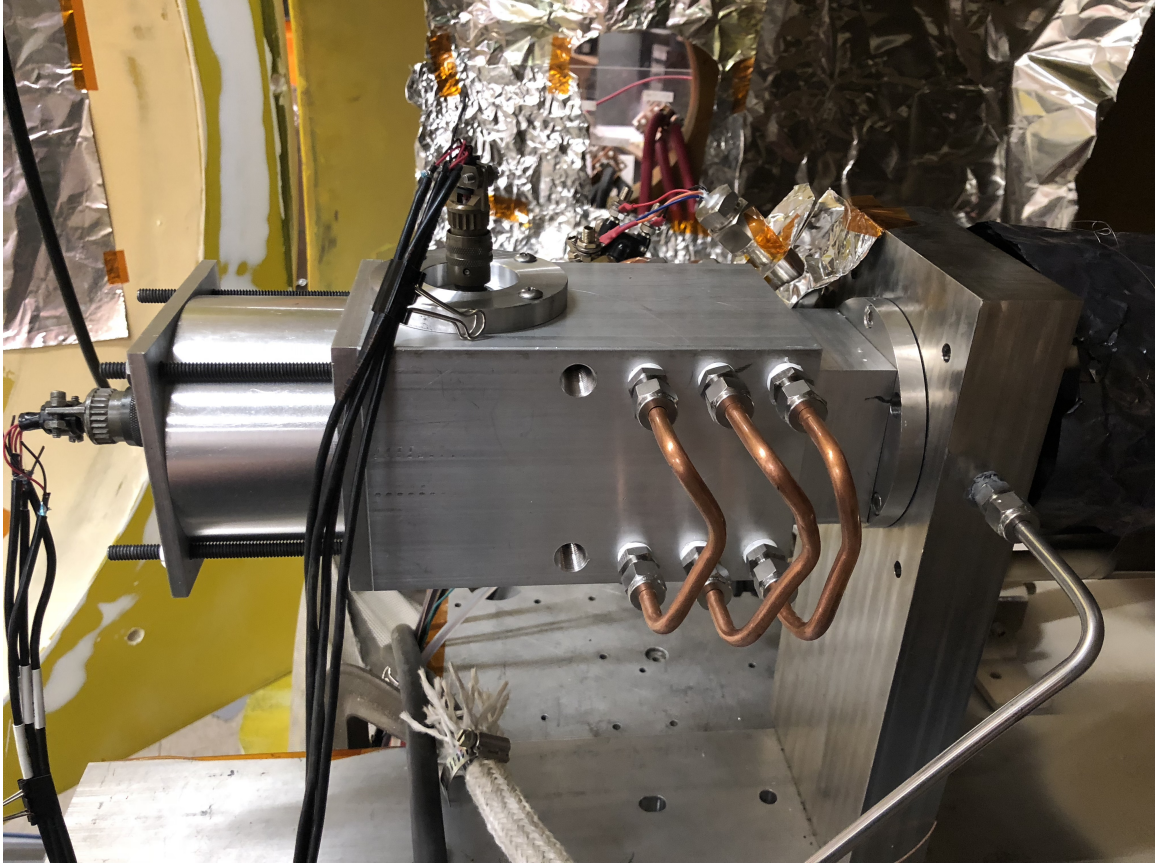


Figure 4.5: The diagnostics assembly after the experiment.

relatively minor, and if given time, could be fixed rather shortly.

The first issue pertains to the mounting procedure of the diagnostics assembly. While CAD modeling, the screw size was assumed to fall well under the $.375''$ diameter for the counterbore. This would allow the screws to be fastened from the side of the hangar step. However, the screw size is just under $.375''$, allowing screws to fit in the holes, but preventing them from being inserted after the diagnostics assembly is built. The screws must be put together with the system, and then fastened together. This makes mounting the system to the base plate unnecessarily difficult and tiring. To fix this issue, four channels should be milled out of the spare material in the aluminum hangar, as shown in Figure 4.6. This would improve the mounting process and modular design considerably.

The wiring within the probe hangar would periodically catch as the probe was extending. As the motor would return, the probe carrier would crowd the probe wires into the rear of the hangar. This region did not have the room for the wire, especially after the mechanical stop was implemented. To fix this issue, the hangar

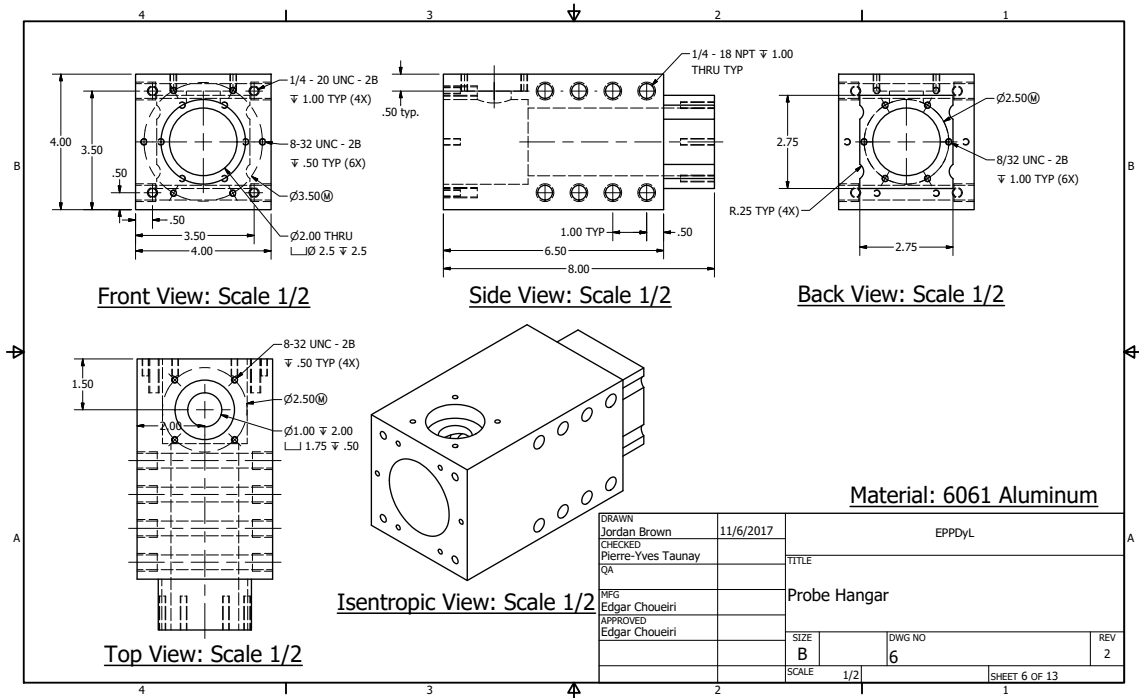


Figure 4.6: Modified probe hanger to improve the wiring and fastening.

diameter should be widened from 2" to 2.5". This diameter change should only be for 3" deep, so as not to interfere with the cooling channels. Figure 4.6 shows what this change would look like. This change would give the wires more space, decreasing the opportunity for them to catch.

As discussed in Section 2.5.1, stepper motors operate through rotating the shaft some discrete number of steps. Providing the motor does not skip steps, the controller is able to track its position at all points in time. By virtue of the sealed chamber, the probe is completely obscured while the fiberglass tank is maintaining vacuum. If the motor were to get caught, there would be no way for an operator to know, which could have damaging effects on the probe or cathode. A string potentiometer or encoder should be added to ensure the position is known for all times.

After experimenting with the motor and controller, a defect was discovered. Querying the motor repeatedly was found to occasionally corrupt the serial commands sent. When this occurs, the motor would accelerate in the direction opposite to the command. This would occur sporadically, with no pattern detectable. Decreasing the query rate would decrease the chance of this bug occurring. Including the string potentiometer would allow greater positional knowledge than the 5 Hz query rate that was used in the experiment.

4.3.2 Conclusion

The diagnostics assembly was successfully implemented into the experimental setup of the EPPDyL. The actuation and structural stability tests met all requirements. There, the device proved moving throughout the active region of an orificed hollow cathode. The device utilizes a leadscrew and vacuum rated stepper motor to linearly actuate a probe suite. A visual control program was programmed in Labview, which allowed the full automation of the system. The probe is capable of traversing a distance of 3.75” and back in 5 seconds.

The device was made out of aluminum and steel, and featured 6 cooling channels. The active cooling and material selection ensured that the steady-state cathode operation did not destroy or deform the diagnostics structure. Two additional channels were included in case more cooling is deemed necessary in the future. Finite element modeling predict that the device can endure emitter temperatures of at least 2500 K, though greater temperatures could be possible. During the experiment, the cathode produced an argon plasma, reaching a temperature of 1600 K.

The cathode was unable to reach steady-state operation, and axial density measurements were unable to be recorded. Further experimentation will be performed once the cathode is fully operational. Minor alterations will be made to the diagnostics to improve their overall performance. The probe hangar shape cavity will be expanded, and several grooves will be made for ease in mounting. A string potentiometer or encoder will also be added to confirm position measurements.

Bibliography

- [1] Riccardo Albertoni, Daniela Pedrini, Fabrizio Paganucci, and Mariano Andrenucci. A reduced-order model for Thermionic hollow cathodes. *IEEE Transactions on Plasma Science*, 41(7):1731–1745, 2013.
- [2] Amphenol Corporation. PT Series: Miniature Cylindrical Connectors, 2016.
- [3] BRITISH STAINLESS STEEL ASSOCIATION. Article: Elevated temperature physical properties of stainless steels.
- [4] Edgar H. Buyco and Fred E. Davis. Specific Heat of Aluminum from Zero to Its Melting Temperature and Beyond Equation for Representation of the Specific Heat of Solids. *Journal of Chemical and Engineering Data*, 15(4):518–523, 1970.
- [5] FF Chen. Langmuir probe diagnostics. . . . -*Course on Plasma Diagnostics, IEEE-ICOPS Meeting, . . .*, page 42, 2003.
- [6] Francis F. Chen. *Introduction to Plasma Physics*. Plenum Publishing Corporation, New York, 1974.
- [7] Bill Earl. All About Stepper Motors. *Adafruit Industries*, pages 1–28, 2015.
- [8] Dan M. Goebel and Emily Chu. High-Current Lanthanum Hexaboride Hollow Cathode for High-Power Hall Thrusters. *Journal of Propulsion and Power*, 30(1):35–40, 2014.
- [9] Dan M. Goebel, Kristina K. Jameson, Ron M. Watkins, Ira Katz, and Ioannis G. Mikellides. Hollow cathode theory and experiment. I. Plasma characterization using fast miniature scanning probes. *Journal of Applied Physics*, 98(11), 2005.
- [10] Dan M. Goebel and Ira Katz. Fundamentals of Electric Propulsion: Ion and Hall Thrusters. *Fundamentals of Electric Propulsion: Ion and Hall Thrusters*, pages 1–507, 2008.

- [11] I. H. Hutchinson. *Principles of Plasma Diagnostics*. Cambridge University Press, New York, second edi edition, 2002.
- [12] Frank P. Incropera, Theodore L. Bergman, Adrienne S. Lavine, and David P. DeWitt. *Fundamentals of Heat and Mass Transfer*. 2011.
- [13] Amir Janjua. Brushed or brushless ? DC motor choices, 2017.
- [14] M. Martinez-Sanchez and J. E. Pollard. Spacecraft Electric Propulsion-An Overview. *Journal of Propulsion and Power*, 14(5):688–699, 1998.
- [15] D. K. Owens. Lecture IV: Langmuir Probes. A Technical Report. Technical report, Princeton Plasma Physics Laboratory, Princeton, 2000.
- [16] Parker Hannifin Corporation. *Parker O-Ring Handbook*, volume 1. Parker, Cleveland, OH, 2012.
- [17] R W Powell, C Y Ho, and P E Liley. Thermal conductivity of selected materials. 1966.
- [18] R. Morrell. Thermal conductivities, 2018.
- [19] Rohit Shastry, Daniel Herman, George Soulas, and Michael Patterson. Status of NASA’s Evolutionary Xenon Thruster (NEXT) Long-Duration Test as of 50,000 h and 900 kg Throughput. *The 33rd International Electric Propulsion Conference*, (March):IECP–2013–121, 2013.
- [20] J E Shigley, C R Mischke, and R G Budynas. *Shigle’s Mechanical Engineering Design - 9th Ed.*, volume New York,. 2002.
- [21] D. SIEGFRIED and P. WILBUR. An investigation of mercury hollow cathode phenomena. *13th International Electric Propulsion Conference*, 1978.
- [22] Gp Sutton and O Biblarz. *Rocket Propulsion Elements*. 2001.
- [23] United Launch Alliance. Delta IV Launch Services User’s Guide. *June*, (June), 2013.
- [24] Christopher J Wordingham, Pierre-yves C R Taunay, and Edgar Y Choueiri. Theoretical Prediction of the Dense-Plasma Attachment Length in an Orificed Hollow Cathode. pages 1–7.

CAD Drawings

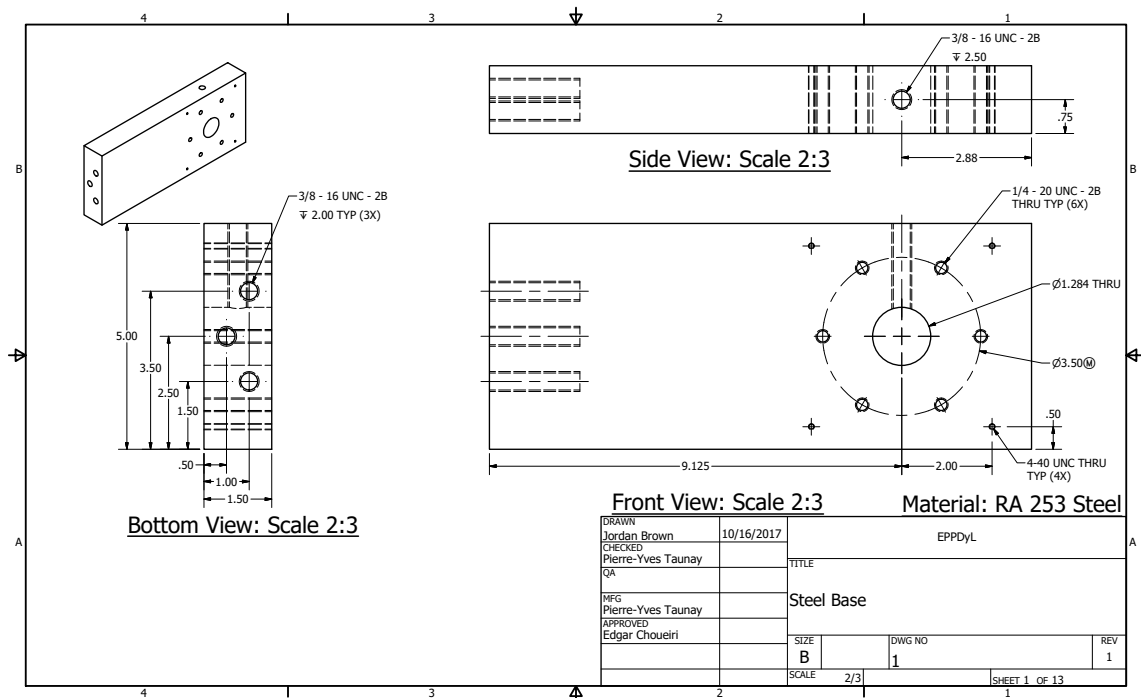


Figure A.1: CAD drawing of the Base Plate

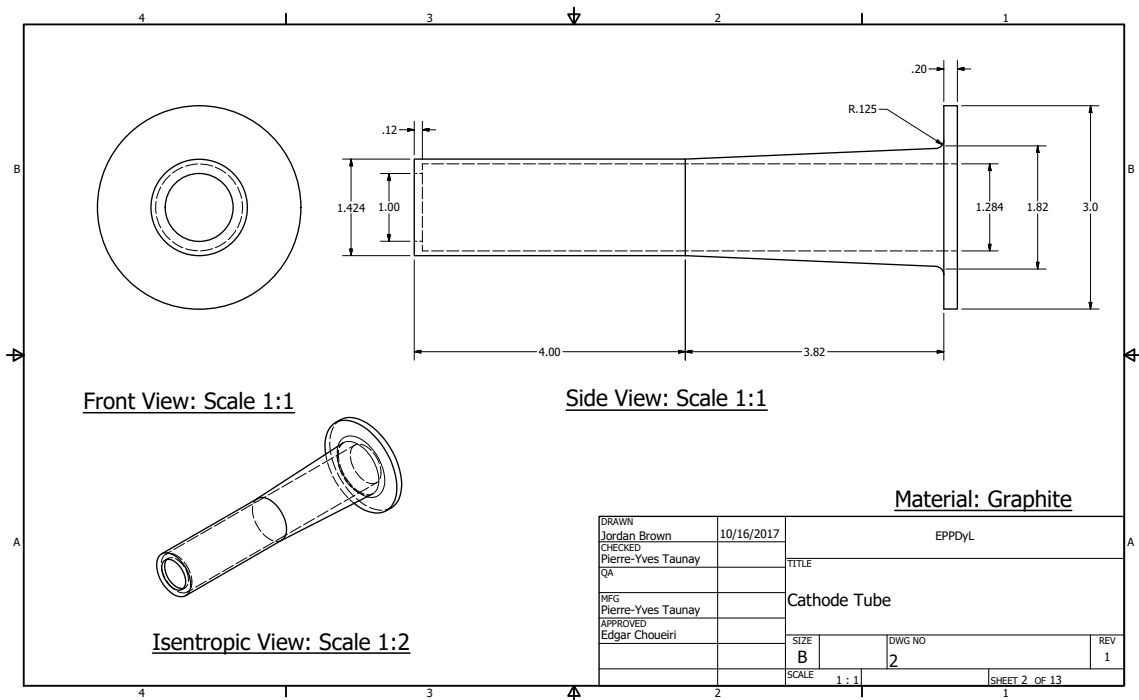


Figure A.2: CAD drawing of a Orificed Hollow Cathode

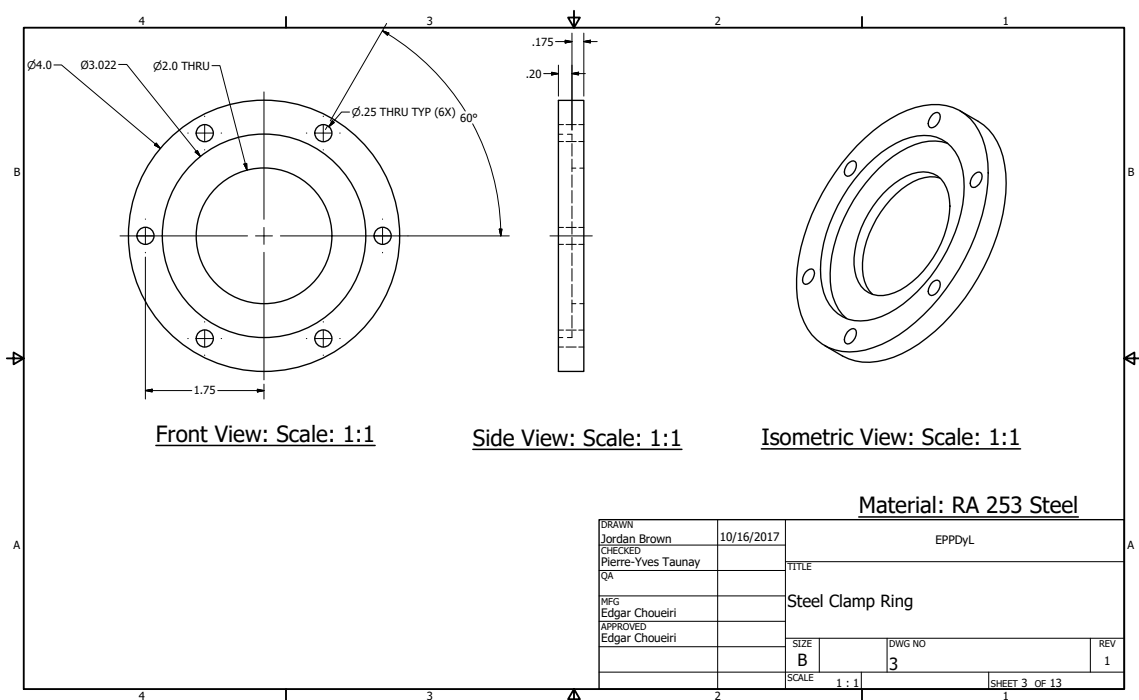


Figure A.3: CAD drawing of the Clamp Ring

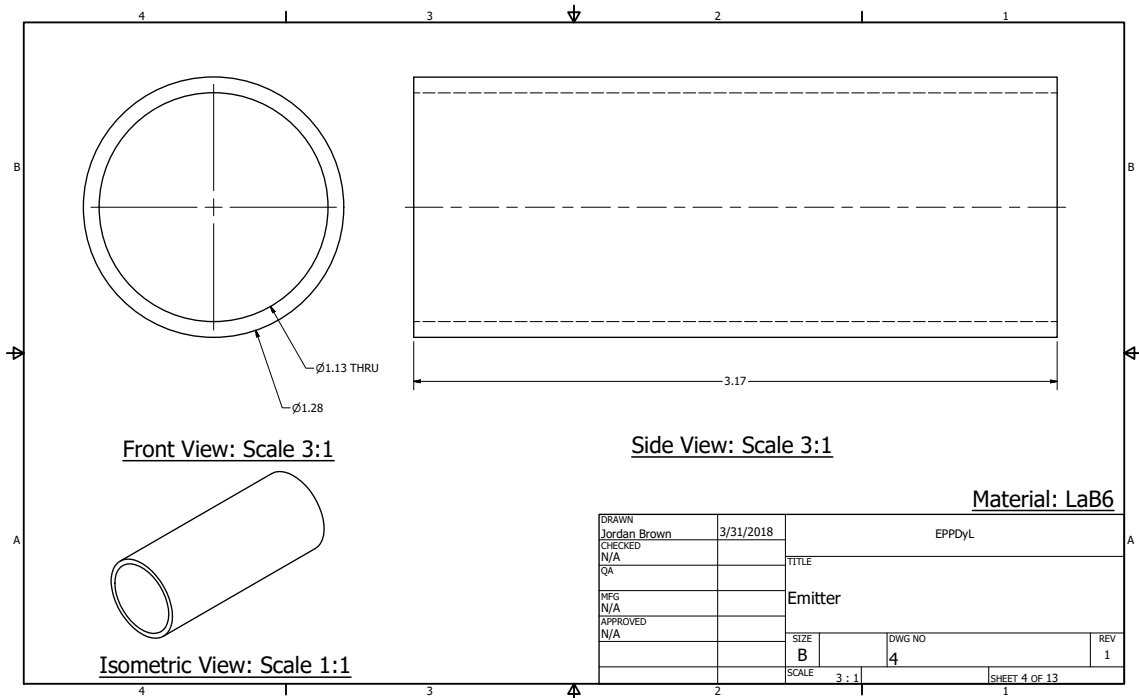


Figure A.4: CAD drawing of the Emitter

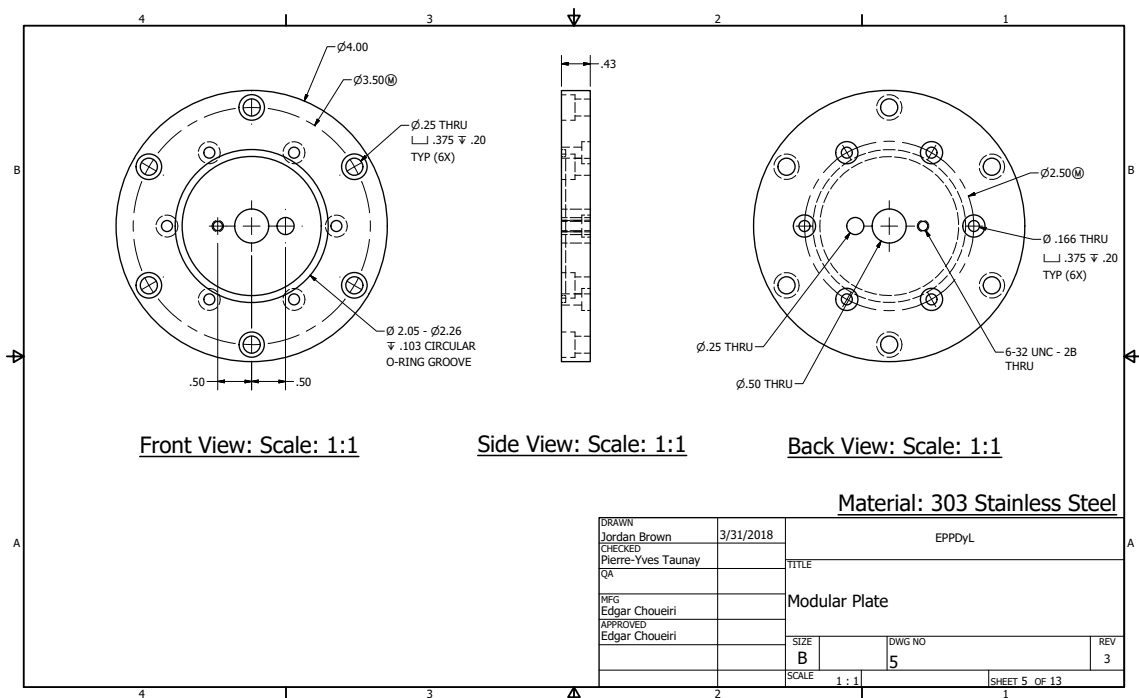


Figure A.5: CAD drawing of the Modular Plate

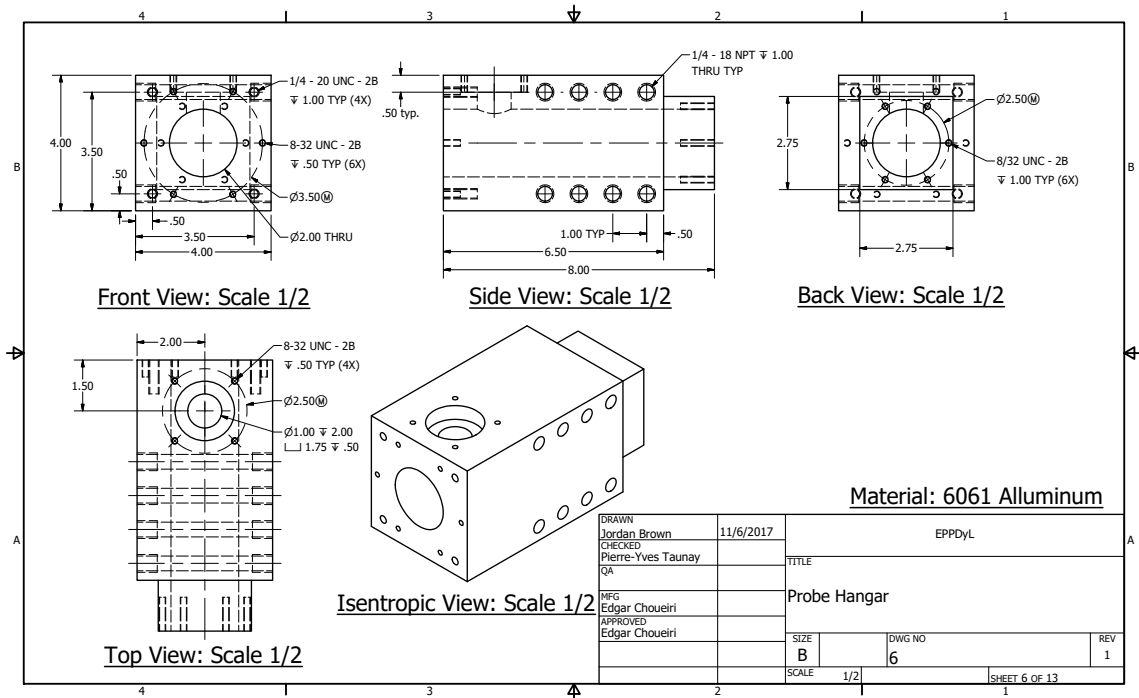


Figure A.6: CAD drawing of the Probe Hangar

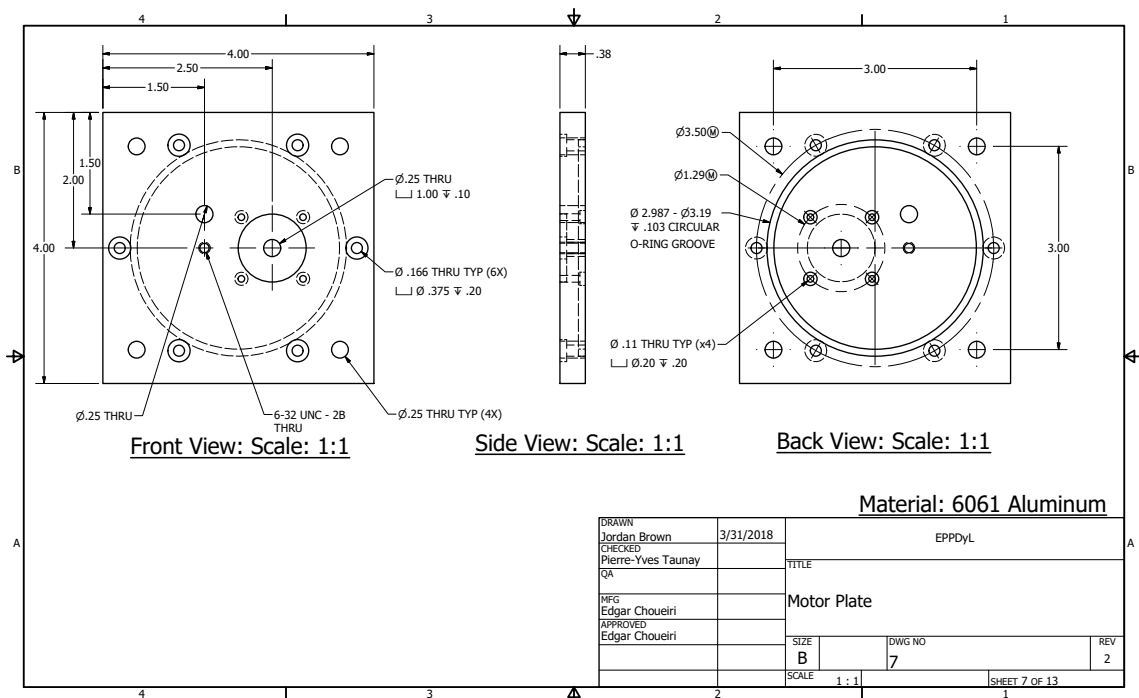


Figure A.7: CAD drawing of the Motor Plate

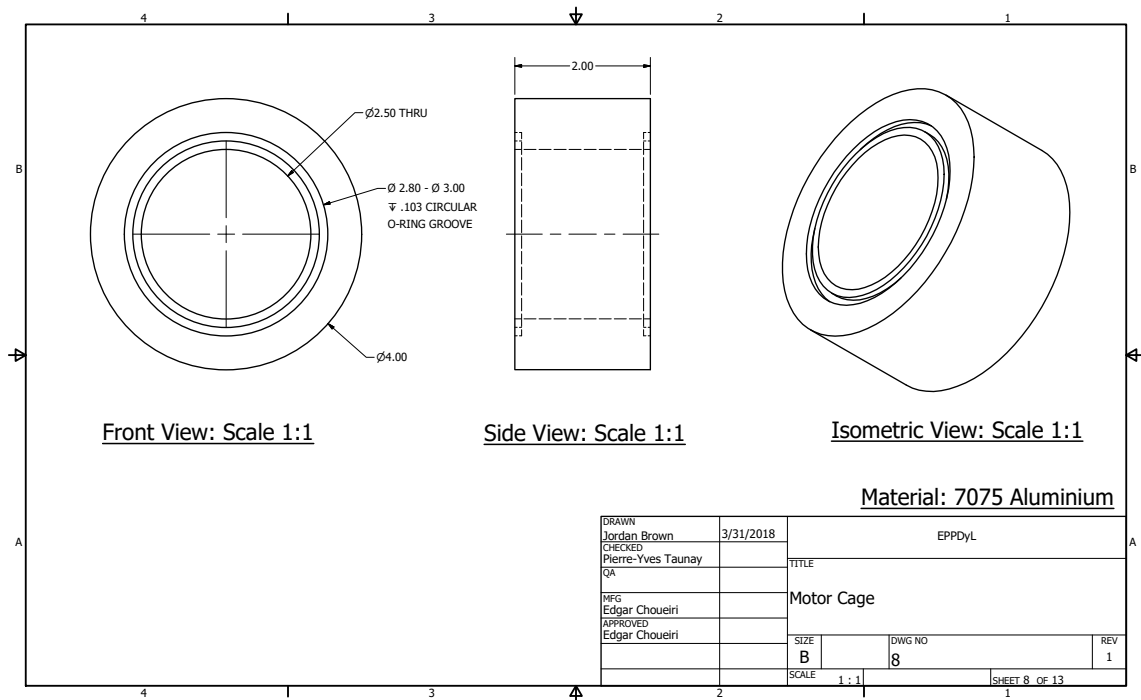


Figure A.8: CAD drawing of the Motor Chamber

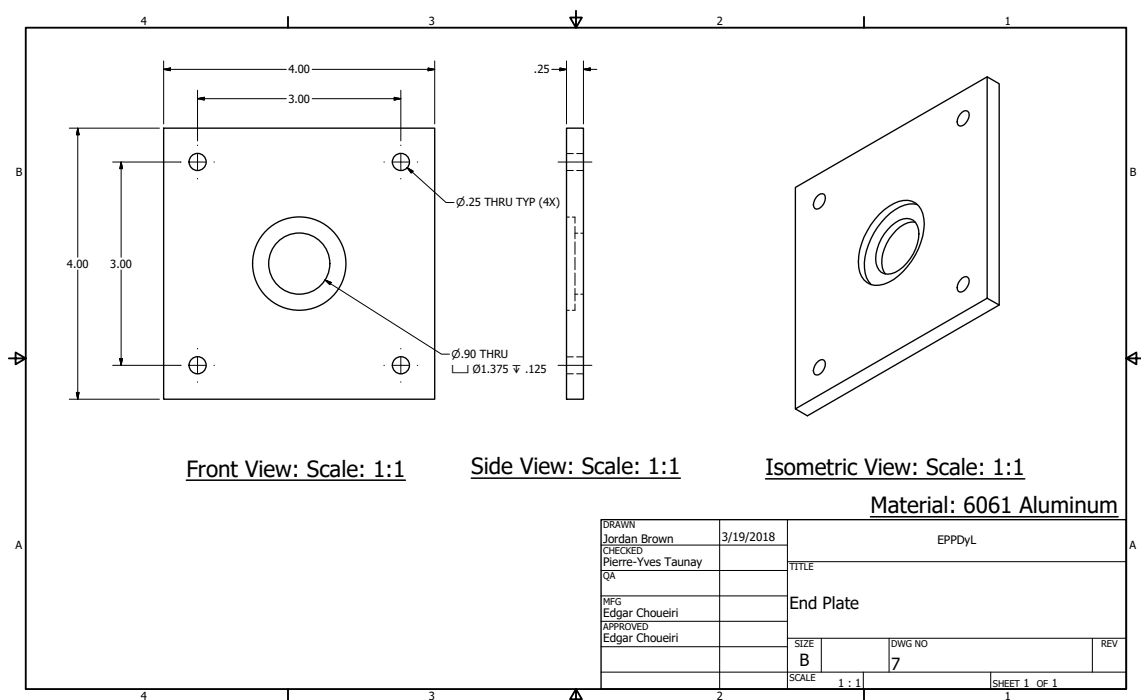


Figure A.9: CAD drawing of the End Plate

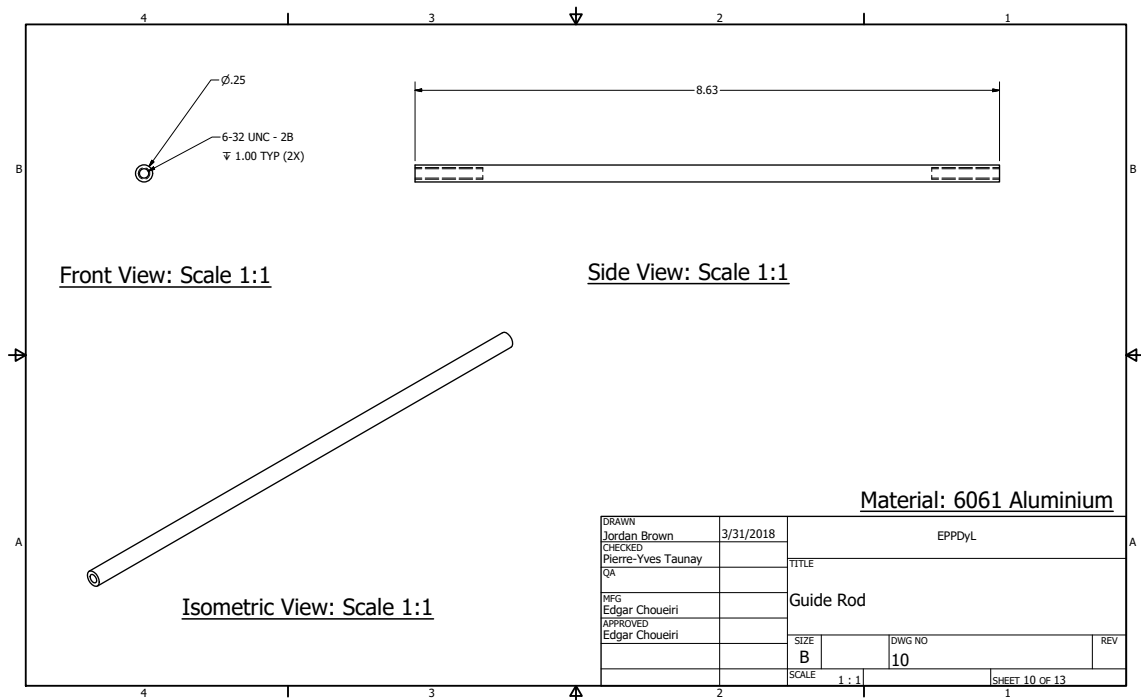


Figure A.10: CAD drawing of the Guide Rod

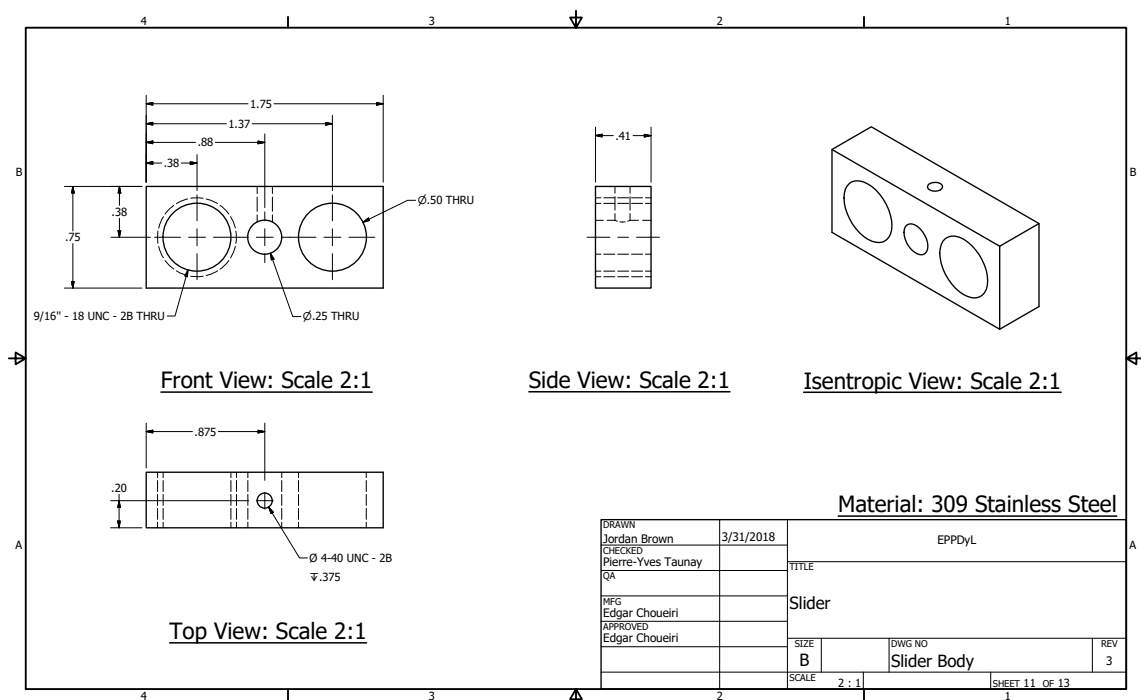


Figure A.11: CAD drawing of the Slider Body

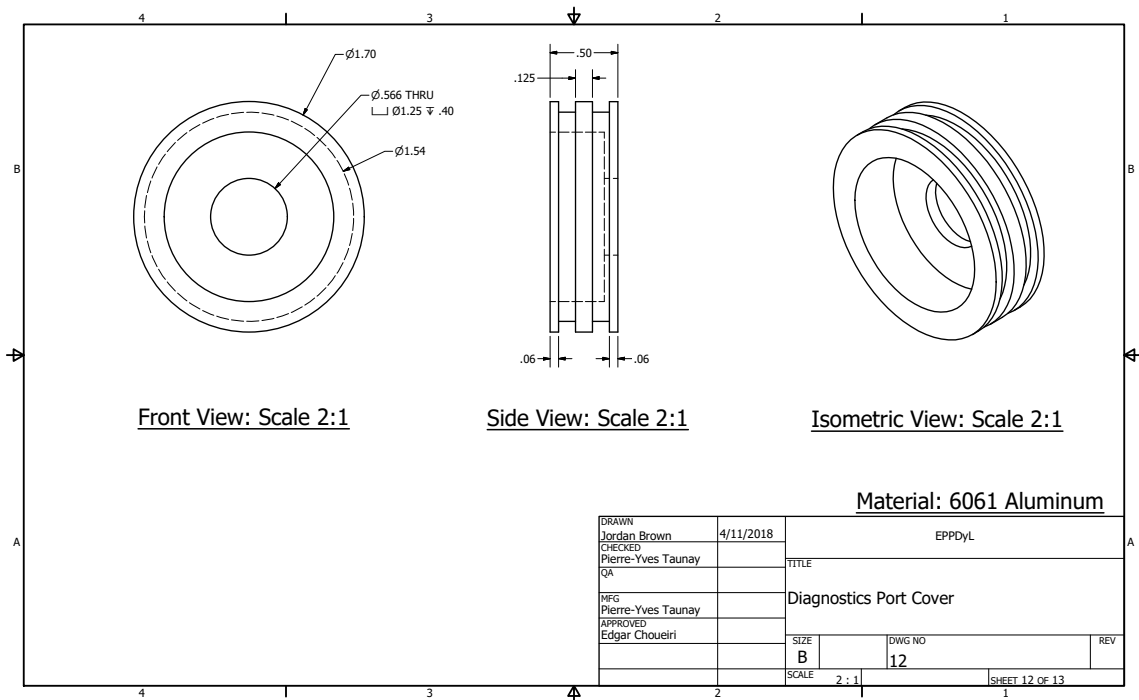


Figure A.12: CAD drawing of the Diagnostics Port Cover

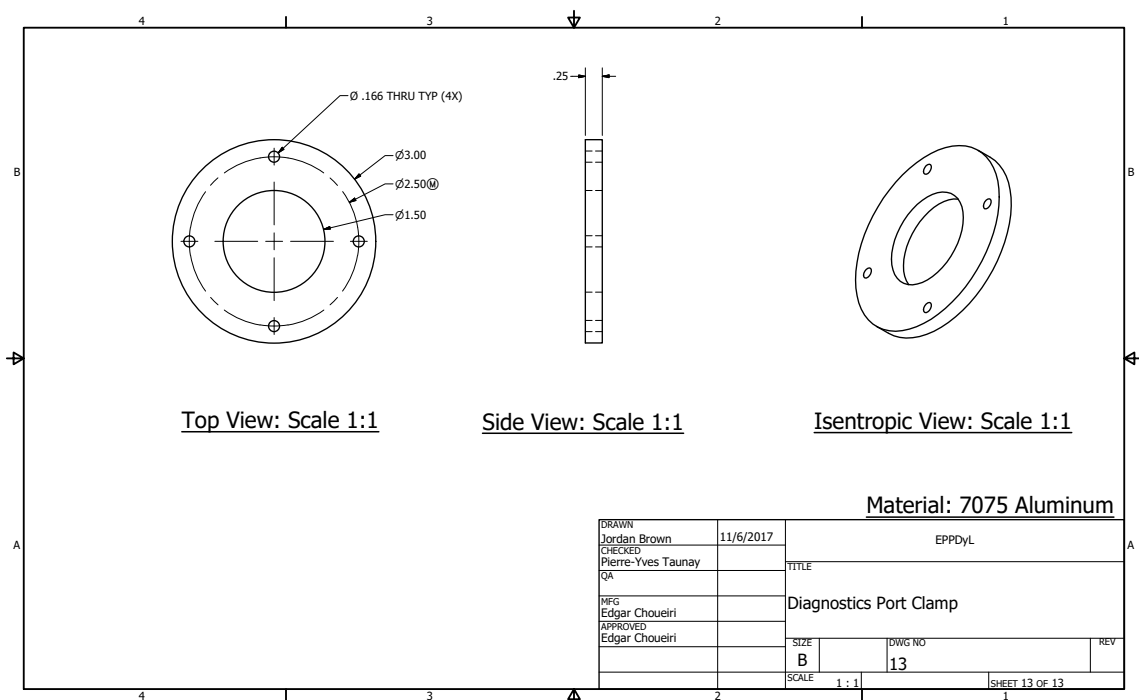


Figure A.13: CAD drawing of the Diagnostics Port Clamp

Appendix B

Motor Schematics

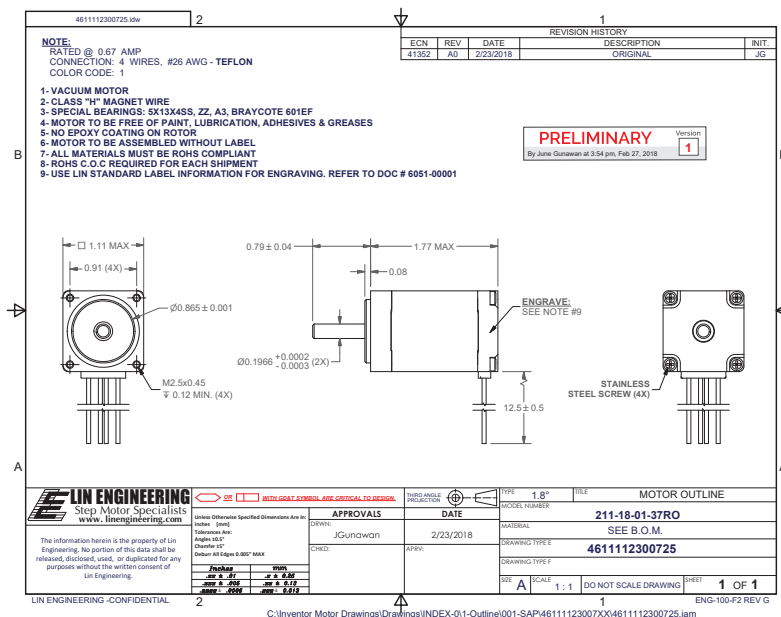


Figure B.1: Engineering Drawing

B.1 Actuation Code

Motor begins at absolute position 0. The controller has a max current of 2 A.

Command String:

/1m30h10j1V5000L10F1z0P11000A0R\r\n

Positional Query:

/1?0

| Command | Explanation |
|---------|---|
| / | Start character command string |
| 1 | Controller Address |
| m30 | Set running current to 30% max (.6 A) |
| h10 | Set holding current to 10% max (.2 A) |
| j1 | Set micro step size to 1 |
| V5000 | Set velocity to 5000 steps/s |
| L10 | Set acceleration to 20 steps/ s^2 |
| F1 | Set motor polarity so positive is counter-clockwise |
| z0 | Set current position as absolute 0 |
| P11000 | Rotate motor 11000 steps in positive direction |
| A0 | Move motor position to 0 |
| R | Run command string |
| \r\n | Execute command for Labview |

Table B.1: Explanation of the command string used to control the stepper motor.

Appendix C

Budget

| Part | Vendor | Price/Part |
|--|---------------|------------|
| 6061 Aluminum, 4" x 4" x 12" | McMaster Carr | 92.96 |
| 6061 Aluminum, 1-3/4" Dia x 1/2" | McMaster Carr | 3.56 (2X) |
| 7075 Aluminum, 3" Dia x 1/4" | McMaster Carr | 13.35 |
| 303 Stainless Steel, 4" Dia x 1/2" | McMaster Carr | 24.62 |
| 6061 Aluminum, 1/4" x 4" x 6" | McMaster Carr | 6.07 |
| 6061 Aluminum, 3/8" X 4" x 6" | McMaster Carr | 8.56 |
| 309 Stainless Steel, 1/4" Dia x 12" | McMaster Carr | 5.88 |
| 304 Stainless Steel, 1/2" x 3/4" x 6" | McMaster Carr | 7.67 |
| Yor-Lok Fittings, 1/4" OD x 1/4 NPT | McMaster Carr | 8.73 (14X) |
| High T. Linear Ball Bearing, 1/4" ID | McMaster Carr | 24.43 (2X) |
| Dry-Running Sleeve Bearing, 1/4" ID | McMaster Carr | 2.58 (2X) |
| Shaft Coupling, 5mm X 1/4" Shaft Dia | McMaster Carr | 43.51 |
| External Retaining Rings, 1/2" OD | McMaster Carr | 9.37 |
| HSS Threaded Rod, 1/4"-20, 3 ft lg. | McMaster Carr | 8.72 |
| 1018 C Steel Leadscrew, 1/4"-16 Thread | McMaster Carr | 9.62 |
| 673 Bronze Round Nut, 1/4"-16 Thread | McMaster Carr | 29.93 (2X) |
| Uncoated HSS 2 Flute End Mill, 1/16" Dia | McMaster Carr | 17.43 |
| Carbide Square-End End Mill, 1/16" Dia | McMaster Carr | 17.36 (2X) |
| Screws, M2.5 X 0.45 mm | McMaster Carr | 8.74 |
| Retaining Ring Plier, 0.038" Dia 90 deg tip | McMaster Carr | 16.15 |
| 18-8 SS Socket Head Screw 1/4"-20, 3/4" lg | McMaster Carr | 9.53 |
| 24" Alumina Tube 4 Bores, 0.188" OD, 0.031" ID | McMaster Carr | 29.10 |

| | | |
|--|-----------------|-----------|
| Neoprene Rubber Sheet, 12" x 24" x 1/32" | McMaster Carr | 12.48 |
| Grafoil, 24" x 24" x 1/32" | McMaster Carr | 62.03 |
| 24" Molybdenum Tube, 0.250 OD x 0.020 wall | McMaster Carr | 212.99 |
| Vacuum Stepper Motor, 211-18-01-37RO | Lin Engineering | 794.00 |
| Stepper Motor Driver, R256-RO | Lin Engineering | 219.30 |
| Isolation Amplifier, AD210BN | Mouser | 116.12 |
| Amphenol Connector, PT07C-8-4S | Amazon | 21.84 |
| Amphenol Connector, PT07C14-19P | Newark | 40.65 |
| Amphenol Connector, PT06A8-4P(SR) | Newark | 22.99 |
| USB to RS485 Converter, DTECH 6 Feet | Amazon | 21.99 |
| Jack Connector, 5 A DC Power Jack | Newark | .708 (5X) |
| USB Receptacle, 2.0 Type B | Newark | .59 |
| Circular Connector, PT06A8-4P(SR) | Newark | 22.29 |
| 5 V Power Supply, LRS-150F-24 | Digi-Key | 25.56 |
| 24 V Power Supply, LRS-150F-5 | Digi-Key | 23.11 |
| Shipping | | 359.81 |
| | Total | 2392.02 |